

AD-A037 303

CERAMIC FINISHING CO STATE COLLEGE PA  
LOCALIZED DAMAGE IN A VISCOUS MEDIUM (GLASS). APPENDIX A. VARIA--ETC(U)  
JAN 77 H P KIRCHNER, R M GRUVER

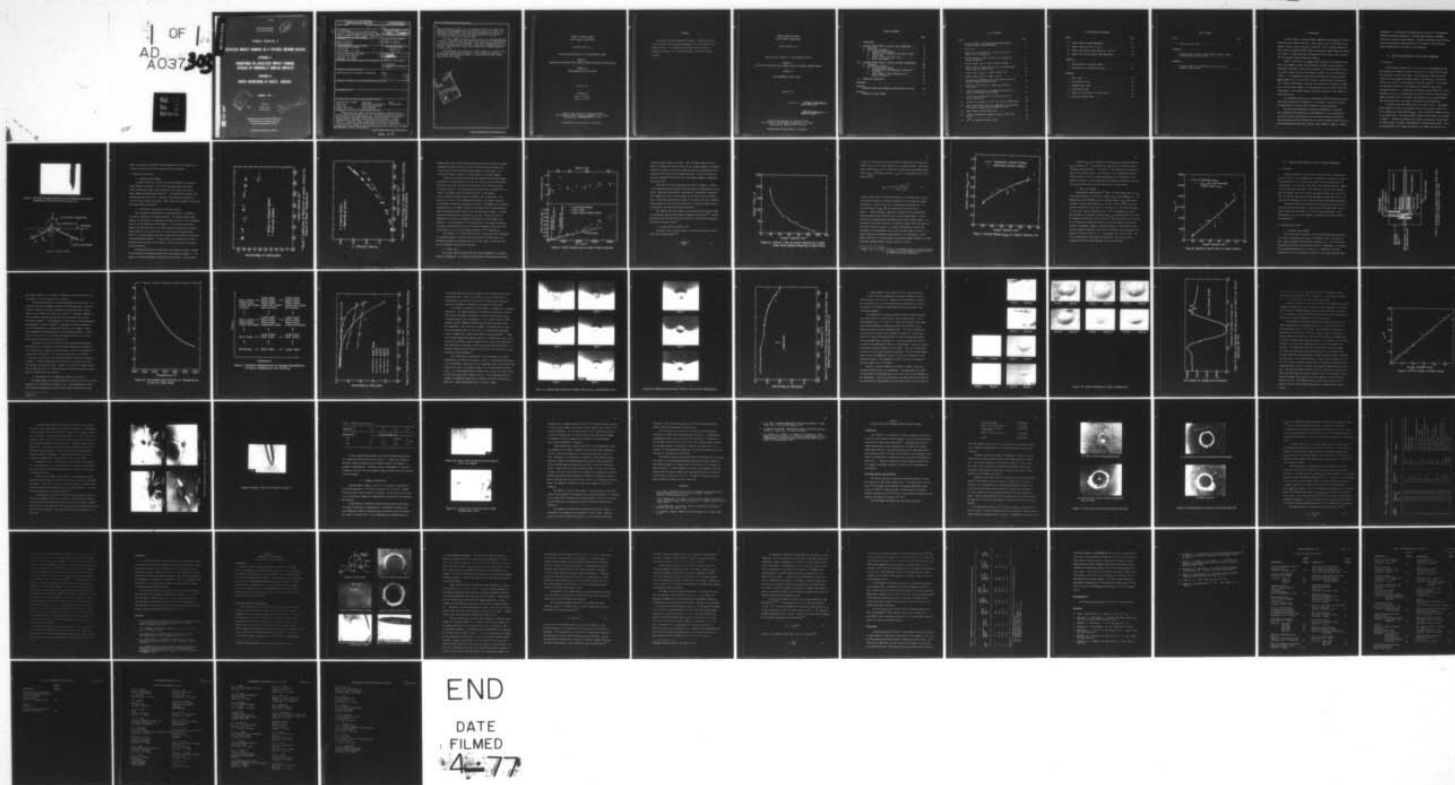
F/G 20/11

N00014-74-C-0241

NL

UNCLASSIFIED

OF 1  
AD  
A037 303



AD.A 037303

Ceramic Finishing Company  
State College, Pennsylvania

TECHNICAL REPORT NO. 5

# LOCALIZED IMPACT DAMAGE IN A VISCOUS M

## APPENDIX A

### VARIATIONS IN LOCALIZED IMPACT D CAUSED BY NOMINALLY SIMILAR IM

## APPENDIX B

### CRACK BRANCHING AT HERTZ CRA

JANUARY, 1977

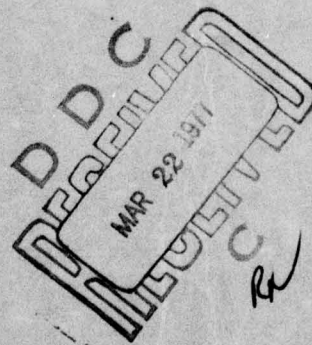
Prepared by:

Henry P. Kirchner  
Robert M. Gruver

Prepared under Contract No. N00014-74-C-0241 for the  
Office of Naval Research, Department of the Navy,  
Requisition No. NR032-545/12-17-73 (471)

Distribution of this document is unlimited.

DDC FILE COPY.



REPORT DOCUMENTATION PAGE		READ INSTRUCTIONS BEFORE COMPLETING FORM
1. REPORT NUMBER	2. GOVT ACCESSION NO.	3. RECIPIENT'S CATALOG NUMBER
4. TITLE (and Subtitle) Localized Damage in a Viscous Medium (Glass). Appendix A, Variations in Localized Impact Damage Caused by Nominally Similar Impacts, Appendix B, Crack Branching at Hertz Cracks.		5. TYPE OF REPORT & PERIOD COVERED Technical Report, no. 5, June 1976 - Jan 1977.
7. AUTHOR(s) Henry P. Kirchner Robert M. Gruver		6. PERFORMING ORG. REPORT NUMBER
9. PERFORMING ORGANIZATION NAME AND ADDRESS Ceramic Finishing Company P.O. Box 498 State College, PA 16801		8. CONTRACT OR GRANT NUMBER(s) N00014-74-C-0241
11. CONTROLLING OFFICE NAME AND ADDRESS Office of Naval Research Department of the Navy Arlington, VA 22217		10. PROGRAM ELEMENT, PROJECT, TASK AREA & WORK UNIT NUMBERS 12/65 P.
14. MONITORING AGENCY NAME & ADDRESS (if different from Controlling Office)		12. REPORT DATE Jan 1977
		13. NUMBER OF PAGES 56
		15. SECURITY CLASS. (of this report) Unclassified
		15a. DECLASSIFICATION/DOWNGRADING SCHEDULE
16. DISTRIBUTION STATEMENT (of this Report) Distribution of this document is unlimited.		
17. DISTRIBUTION STATEMENT (of the abstract entered in Block 20, if different from Report) DISTRIBUTION STATEMENT A Approved for public release; Distribution Unlimited		
18. SUPPLEMENTARY NOTES		
19. KEY WORDS (Continue on reverse side if necessary and identify by block number) localized impact damage      penetration      glass Hertz crack      coefficient of restitution      viscous medium radial crack      energy loss mechanisms lateral vent crack      crack branching		
20. ABSTRACT (Continue on reverse side if necessary and identify by block number) Glass plates were lightly abraded and impacted by glass spheres at various velocities and temperatures. The incoming and rebounding velocities were measured by high speed photography. The coefficients of restitution, kinetic energies and kinetic energy losses were calculated. At room temperatures the coefficient of restitution decreases with increasing velocity. The kinetic energy losses appear to increase linearly with increasing kinetic energy at low velocities but at higher velocities the		



↓  
losses increase at a faster rate. This greater increase may result from additional loss mechanisms associated with fracturing of the surface. At temperatures above 580°C viscous flow permits indentation of the surface. The losses associated with the viscous flow reduce the coefficient of restitution over the entire velocity range.

The impact damage was characterized by optical and scanning electron microscopy. Typically, the ring cracks show extensive crack branching which is clearly revealed in etched specimens. The crack branching was used to locate the fracture origin of the Hertz cracks and to estimate the fracture stresses. These fracture stresses were compared with estimates based on the Hertz theory.

Forty specimens were subjected to similar impacts at a velocity near the threshold for Hertz crack formation. Hertz cracks were observed in approximately half of these specimens. The penetration of these cracks varied over a wide range.  
↑

COPIES FOR

NTIS ☒ White Section ☐  
 DOC ☐ Buff Section ☐

UNANNOUNCED  
JUSTIFICATION

BY ☐ DISTRIBUTION/AVAILABILITY CODES  
 Dist. ☐ AVAIL. and/or SPECIAL

PA



CERAMIC FINISHING COMPANY  
STATE COLLEGE, PENNSYLVANIA

Technical Report No. 5

LOCALIZED IMPACT DAMAGE IN A VISCOUS MEDIUM (GLASS)

APPENDIX A  
VARIATIONS IN LOCALIZED IMPACT DAMAGE CAUSED BY NOMINALLY SIMILAR IMPACTS

APPENDIX B  
CRACK BRANCHING AT HERTZ CRACKS

January, 1977

Prepared by:  
Henry P. Kirchner  
Robert M. Gruver

Prepared under Contract No. N00014-74-C-0241  
for the Office of Naval Research, Department of the Navy,  
Requisition No. NR032-545/12-17-73 (471)

Distribution of this document is unlimited.

## FOREWARD

This report describes research performed on a program sponsored by the office of Naval Research, Department of the Navy under Contract N00014-74-C-0241. The research was performed under the general technical direction of Dr. Arthur M. Diness of the Office of Naval Research.

CERAMIC FINISHING COMPANY  
STATE COLLEGE, PENNSYLVANIA

Technical Report No. 5

LOCALIZED IMPACT DAMAGE IN A VISCOUS MEDIUM (GLASS)

APPENDIX A

VARIATIONS IN LOCALIZED IMPACT DAMAGE CAUSED BY NOMINALLY SIMILAR IMPACTS

APPENDIX B

CRACK BRANCHING AT HERTZ CRACKS

January, 1977

Prepared by:

Henry P. Kuehner  
Henry P. Kirchner

Robert M. Gruver  
Robert M. Gruver

Prepared under Contract No. N00014-74-C-0241  
for the Office of Naval Research, Department of the Navy,  
Requisition No. NR-32-545/12-17-73 (471)

Distribution of this document is unlimited.



## TABLE OF CONTENTS

	Page
I. INTRODUCTION . . . . .	1
II. LOCALIZED IMPACT DAMAGE IN GLASS AT ROOM TEMPERATURE . . .	2
A. Procedures . . . . .	2
B. Results and Discussion . . . . .	4
1. Localized impact damage . . . . .	4
2. Coefficient of restitution and kinetic energy . .	4
3. Contact time . . . . .	7
4. Contact radius and impact force . . . . .	9
5. Hertz cone lengths . . . . .	13
III. LOCALIZED IMPACT DAMAGE IN GLASS AT ELEVATED TEMPERATURES .	15
A. Procedures . . . . .	15
B. Results and Discussion . . . . .	15
1. Localized impact damage . . . . .	15
2. Determination of the indentation temperature at 50 ms <sup>-1</sup> . . . . .	17
3. Impact damage at high temperatures and various velocities . . . . .	25
IV. SUMMARY AND CONCLUSIONS . . . . .	34
REFERENCES . . . . .	37
APPENDIX A	
LOCALIZED DAMAGE FROM NOMINALLY SIMILAR IMPACTS ON GLASS .	39
APPENDIX B	
BRANCHING OF HERTZ CRACKS . . . . .	47

# LIST OF FIGURES

Figure		Page
1	Multiple images of incoming and rebounding spheres, obtained by high speed photography . . . . .	3
2	Hertz crack . . . . .	3
3	Coefficient of restitution vs. impact velocity for impacts at room temperature . . . . .	5
4	Kinetic energy vs. impact velocity for incoming and rebounding spheres . . . . .	6
5	Kinetic energy loss vs. impact velocity squared . . . . .	8
6	Contact time vs. impact velocity for a 3 mm diam glass sphere impacting a glass plate . . . . .	10
7	Contact radius ( $a_{max}$ ) vs. impact velocity (V) . . . . .	12
8	Maximum impact force vs. impact velocity . . . . .	14
9	Experimental arrangement used to heat glass plates for elevated temperature impact tests . . . . .	16
10	Estimated log viscosity vs. temperature curve for float glass . . . . .	18
11	Schematic representation of damage characteristics at various temperatures and velocities . . . . .	19
12	Coefficient of restitution vs. impact velocity at various temperatures . . . . .	20
13	Indentations observed at $50 \text{ ms}^{-1}$ and various temperatures .	22
14	Coefficient of restitution vs. temperature for 3 mm diam glass spheres impacting glass plates at $50 \text{ ms}^{-1}$ . . . . .	24
15	Impact damage at high temperatures . . . . .	26
16	Profile of indentation formed by impact at $700^\circ\text{C}$ and $74 \text{ ms}^{-1}$ . . . . .	28
17	$aV^{6/5}$ vs. number of radial cracks . . . . .	30

# LIST OF FIGURES (continued)

Figure		Page
18	Radial cracks at high temperatures . . . . .	32
19	Radial crack tip (770°C, 57 ms <sup>-1</sup> ) . . . . .	33
20	Sharp crack extending from elliptical crack tip . . . . .	35
21	Lateral vent crack formed at high temperature . . . . .	35

## APPENDIX A

1	Characteristics of surface cracks . . . . .	41
2	Intersections of cracks with surface . . . . .	42

## APPENDIX B

1	Hertz crack . . . . .	48
2	Partial Hertz crack . . . . .	48
3	Complete Hertz crack . . . . .	48
4	Spiral Hertz crack . . . . .	48
5	Hackle on the surface of the cone crack . . . . .	48
6	Side view of Hertz cone . . . . .	48



## LIST OF TABLES

Table	Page
I Radial crack tip radii . . . . .	34
APPENDIX A	
I Characteristics of Hertz cracks formed by similar impacts of glass spheres on glass plates . . . . .	44
APPENDIX B	
I Estimated fracture stress and flaw size for fracture origins of Hertz cracks . . . . .	54

## I. INTRODUCTION

Two basic types of localized impact damage have been observed in brittle materials at low impact velocities. Blunt objects, such as relatively large diameter spheres, cause formation of Hertz cone cracks. Smaller spheres and sharp particles (abrasive grain) indent the surfaces forming radial and lateral vent cracks. At high velocities both sharp and blunt objects cause crushing and the fracture patterns become very complex.

Evans<sup>(1)</sup> showed that, for static contact stresses, the transition from Hertz crack damage to radial crack formation, observed in materials with decreasing brittleness, results from a decrease in the radial tensile stress ( $\sigma_{11}$ ) and a change in sign of the tangential stress ( $\sigma_{22}$ ) from compressive to tensile. It is desirable to extend these observations to include localized impact damage, but it is difficult to obtain a suitable series of materials with a range of brittleness. To avoid this problem it was decided to investigate localized impact damage in a viscous medium; that is, glass at elevated temperatures. This decision permits continuous variation of the tendency to deform under load.

The mechanical properties of viscous media differ from those of plastic media mainly because of the absence of a yield point. Care must be used in the application of concepts such as hardness to viscous materials.

The next section describes a detailed investigation of localized impact damage in soda-lime glass at room temperature. This investigation was used to develop techniques for the later high temperature work and to obtain base-line data for the material in a brittle condition (high viscosity). The following section describes localized impact damage in glass at elevated

temperatures. Two additional investigations are reported in the Appendices. Appendix A describes variations in localized impact damage in specimens subjected to nominally similar impacts. Appendix B describes crack branching at Hertz cracks and includes estimates of the stresses at which the Hertz cracks formed based on the radii at crack branching.

## II. LOCALIZED IMPACT DAMAGE IN GLASS AT ROOM TEMPERATURE

### A. Procedures

PPG float glass plates ( $1/4 \times 1-1/4 \times 1-1/4$  in) were abraded on the side opposite that formed in contact with the tin by dropping -80 +150 mesh SiC grain from a height of one meter. The plates were firmly supported by a steel block and impacted by glass spheres, 3 mm diameter, at velocities ranging up to  $138 \text{ ms}^{-1}$ , as described in a previous report<sup>(2)</sup>. The incoming and rebounding velocities of the spheres were measured by high speed photography (Figure 1). An electronic stroboscope (General Radio No. 1538-A), flashing at rates up to 150,000 times per minute was used to obtain multiple images on Polaroid film. To improve the reflectivity of the glass spheres, they were coated with a thin layer of aluminum by vacuum deposition.

The glass plates were coated with a thin layer of soot. The impression, formed in the soot by the impact, was used to locate the impact site and to measure the contact radius ( $a_{\text{max}}$ ). Hertz cracks were observed at most of the impact sites. The symbols used to describe these cracks are indicated in Figure 2. The soot was removed and the Hertz crack radius and the radii of radial cracks, if present, were measured in the underlying surface. Then, the specimens were cut through the center of the impact site and the cone



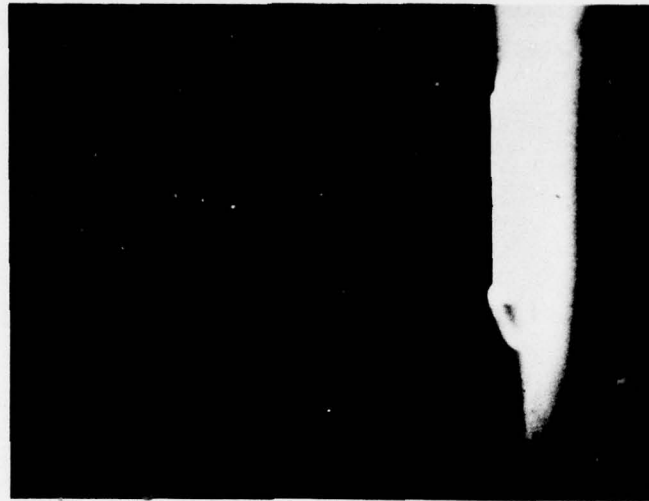


Figure 1 Multiple Images of Imcoming and Rebounding Spheres  
Obtained by High Speed Photography (IX)

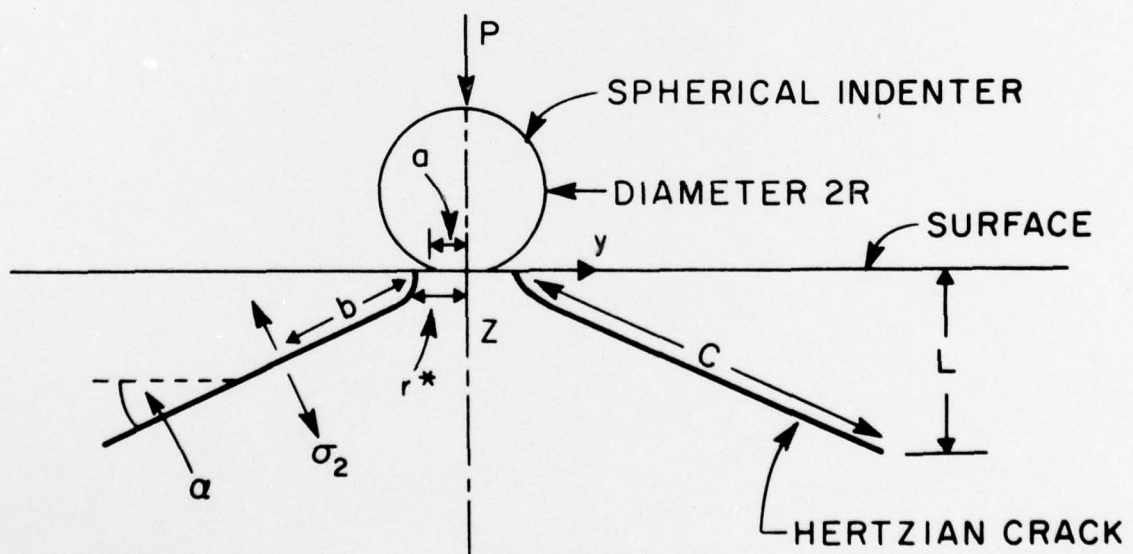


Figure 2 Hertz Crack

angle ( $\alpha$ ) and Hertz crack depth ( $L$ ) were measured on the cut surface or by focusing a microscope into the specimen from the cut surface.

## B. Results and Discussion

### 1. Localized impact damage

At impact velocities up to  $28 \text{ ms}^{-1}$  (nine specimens), no localized impact damage was observed. At  $30.6 \text{ ms}^{-1}$  and above Hertz cracks were formed in almost all cases. Hertz cracks and other types of localized impact damage were described previously<sup>(2)</sup>. The threshold for radial crack formation was about  $56.1 \text{ ms}^{-1}$ . Crushing of the surface was observed at  $125.8 \text{ ms}^{-1}$  and at higher velocities. These results are reasonably consistent with those reported earlier<sup>(2)</sup>.

### 2. Coefficient of restitution and kinetic energy

The coefficient of restitution of impacting bodies is a measure of the elastic efficiency of the impact process. For impacts against rigid targets, the coefficient of restitution is simply the ratio of the rebounding velocity to the incoming velocity (Figure 3). It is evident from these results that the efficiency of the impact process decreases with increasing impact velocity, but at a slow rate. In a few cases at velocities over  $120 \text{ ms}^{-1}$ , the glass spheres fractured on impact and low values of coefficient of restitution were observed. In these cases, the rebound velocities were measured on only one piece of the sphere. Other pieces may have rebounded at other velocities.

The masses and velocities were used to calculate the kinetic energies of the incoming and rebounding spheres which are compared in Figure 4. The results for fractured spheres are omitted from this figure. The difference

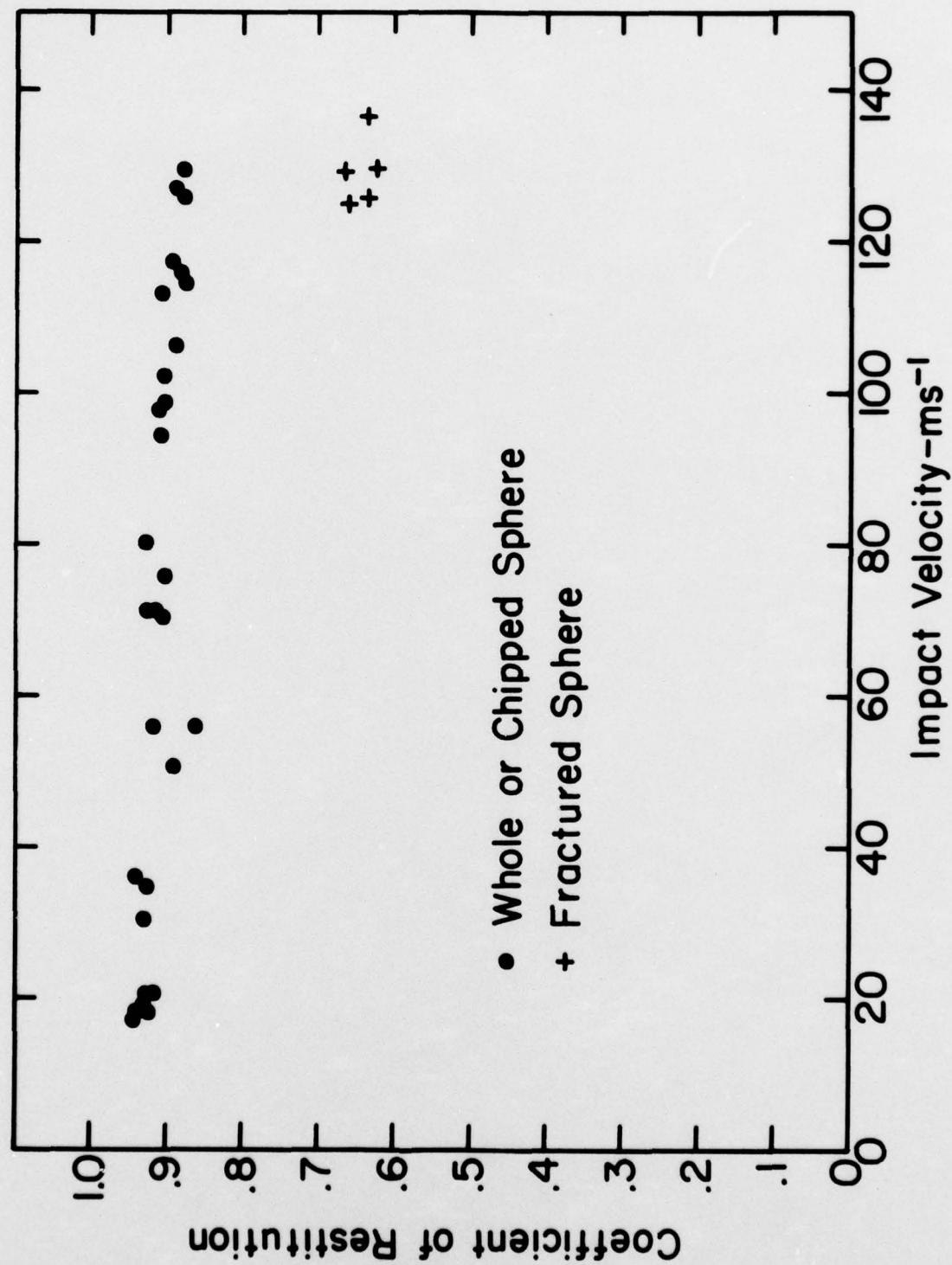


Figure 3 Coefficient of Restitution vs. Impact Velocity for Impacts at Room Temperature



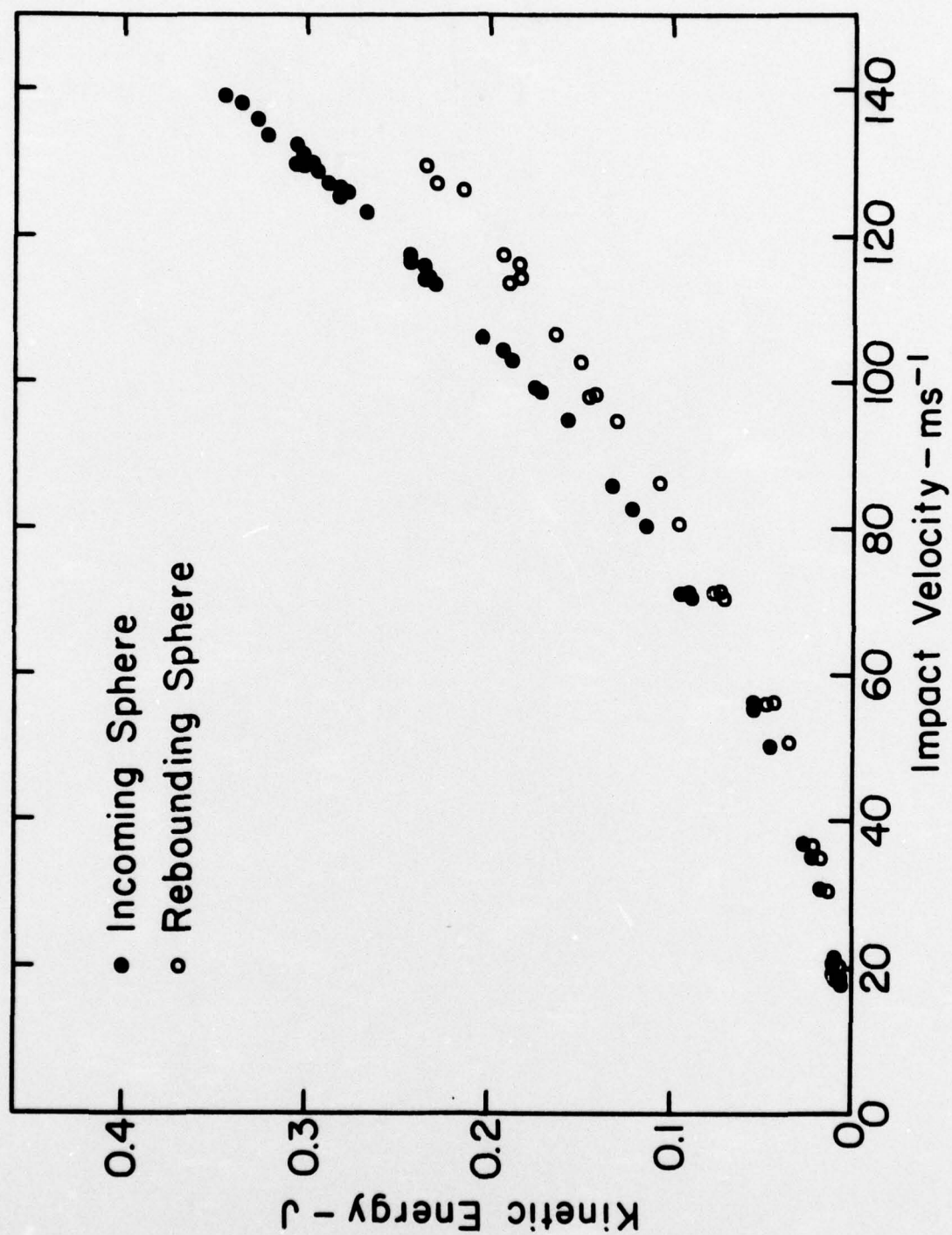


Figure 4 Kinetic Energy vs. Impact Velocity for Incoming and Rebounding Spheres

between these curves is the kinetic energy loss which may consist of several components including stress wave energy, elastic deflection energy of the target, and the fracture surface energy required to form cracks. It is of obvious interest to relate the energy losses to the impact damage.

Losses such as stress wave energy and target deflection energy might be expected to be proportional to the kinetic energy of the incoming spheres. Therefore, the kinetic energy loss was plotted vs. the velocity squared as shown in Figure 5. The resulting curve diverges from a straight line, at least at the higher velocities indicating that, in the higher velocity range, the losses increase at greater than a linear rate. The losses are 11-16% of the incoming kinetic energy at low impact velocities and increase to 20-22% at the highest velocities. The weight of the evidence suggests that, at low impact velocities, the losses due to stress waves and target deflection increase linearly with incoming kinetic energy. At higher velocities another factor contributes to the loss. This factor may be indentation or a factor coinciding with indentation such as radial crack formation. A second possibility is that the onset of the higher percentage of losses coincides with the onset of extensive branching of the ring crack which begins to occur at impact velocities under  $60 \text{ ms}^{-1}$  (Appendix B).

The presence of two high values of kinetic energy loss in the threshold or transition region of the curve raises the question whether there is an additional mechanism or mechanisms of loss in this region. Sufficient data are not available to resolve this question.

### 3. Contact time

The contact time was measured by high speed photography in a separate series of experiments. The incoming and rebounding velocities were determined

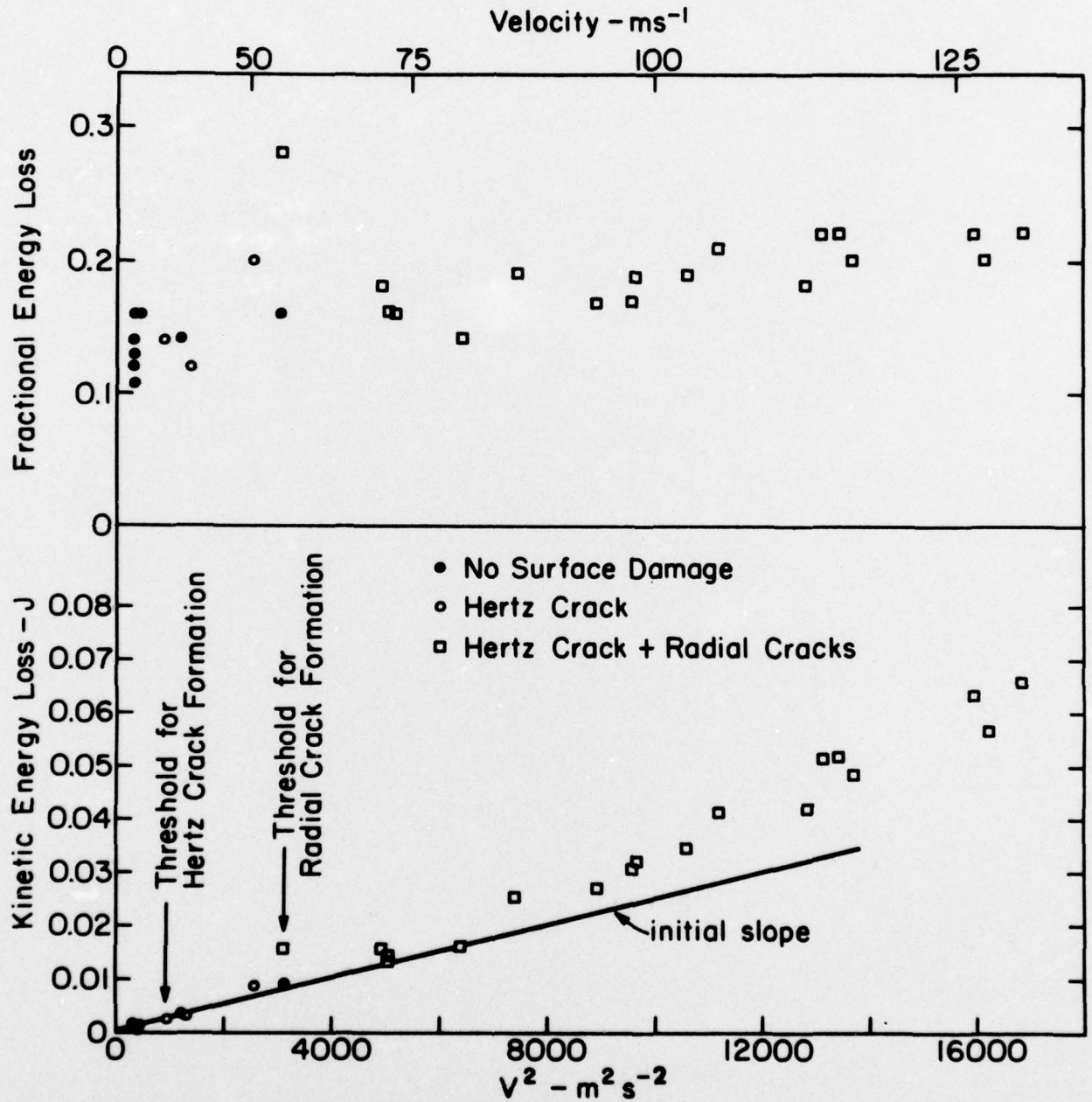


Figure 5 Kinetic Energy Loss vs. Impact Velocity Squared



from the multiple images, as before. Then, the times required for the sphere to traverse the distance from the last incoming image to the surface and from the surface to the first outgoing image were calculated from the respective velocities and the measured distances. The sum of these two times was subtracted from 400  $\mu$ s (the time between flashes) to determine the contact time.

The results of these measurements are given in Figure 6. Results at the lowest velocities have been omitted because of uncertainties in the values. When the contact time is long there is a substantial probability that flashes will occur while the sphere is in contact with the surface. Also, the spacings become small relative to the size of the spot reflected from the sphere so that the errors involved in locating the sphere can be a substantial fraction of the distance traversed.

The contact times were larger at low velocities than expected based on calculations using the equations of Timoshenko and Goodier<sup>(3)</sup>. Similar deviations from the theory have been observed for steel spheres impacting relatively thin steel plates<sup>(4)</sup>.

#### 4. Contact radius and impact force

The Hertz theory provides a means to calculate the contact radius using the following equation<sup>(5)</sup>

$$a = \left( \frac{4QPR}{3E_1} \right)^{1/3} \quad (1)$$

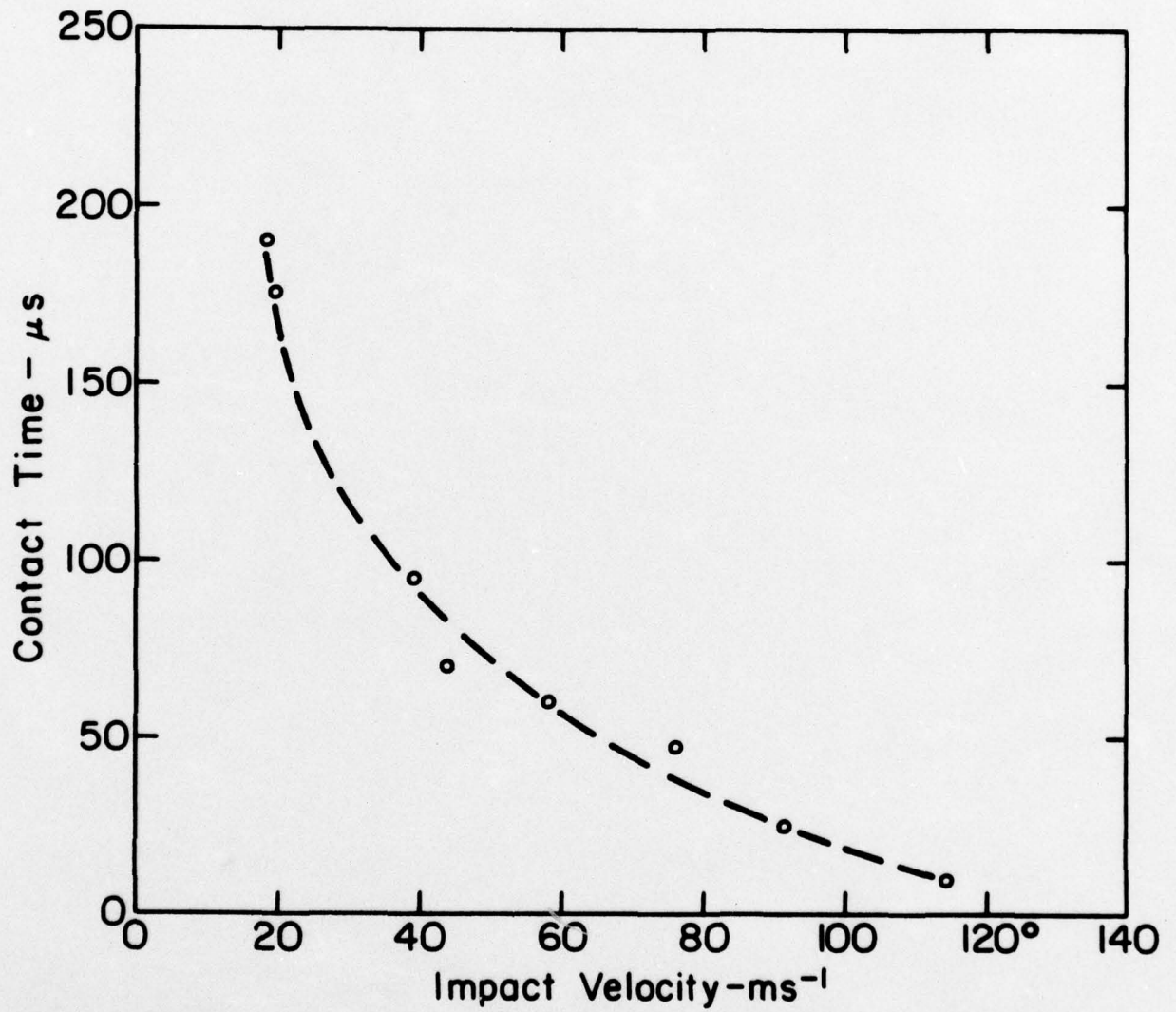


Figure 6 Contact Time vs. Impact Velocity for a 3mm  
Diam. Glass Sphere Impacting a Glass Plate

in which  $Q$  is a factor involving the elastic properties of the sphere and target<sup>\*</sup> and  $E_1$  is the Young's modulus of the target material. The maximum contact radius ( $a_{\max}$ ) can be calculated by substituting the maximum impact force ( $P_{\max}$ ) in the above equation.  $P_{\max}$  can be calculated from the Hertz theory using<sup>(5)</sup>

$$P_{\max} = 1.52 R^2 \left[ \frac{\pi V^6 \rho^3}{(k_1 + k_2)^2} \right]^{1/5} \quad (2)$$

in which  $V$  and  $\rho$  are the velocity and density of the sphere and  $k_1$  and  $k_2$  are constants related to the elastic properties of the target and sphere respectively. Values of  $P_{\max}$  were calculated and substituted in (1) to calculate values of  $a_{\max}$  which are indicated by the solid line in Figure 7. These theoretical values were compared with the experimental values, revealing some variations from the theoretical values. At low velocities, the measured and calculated contact radii nearly coincide. At velocities in the range 35-60 ms<sup>-1</sup> the measured contact radii fall above the curve but, looking at the data as a whole, this appears to result from flattening of the experimental curve in the velocity range 35-80 ms<sup>-1</sup>. At higher velocities the measured values appear to be increasing at a rate greater than that of the theoretical curve perhaps because formation of radial cracks and crushing permits a greater radius of contact.

\*  $Q = \left[ \frac{9}{16} (1-\nu_1^2) + (1-\nu_2^2) \frac{E_1}{E_2} \right]$  in which  $\nu$  is Poisson's ratio,  $E$  is Young's modulus of elasticity and the subscripts 1 and 2 refer to the target and sphere, respectively.



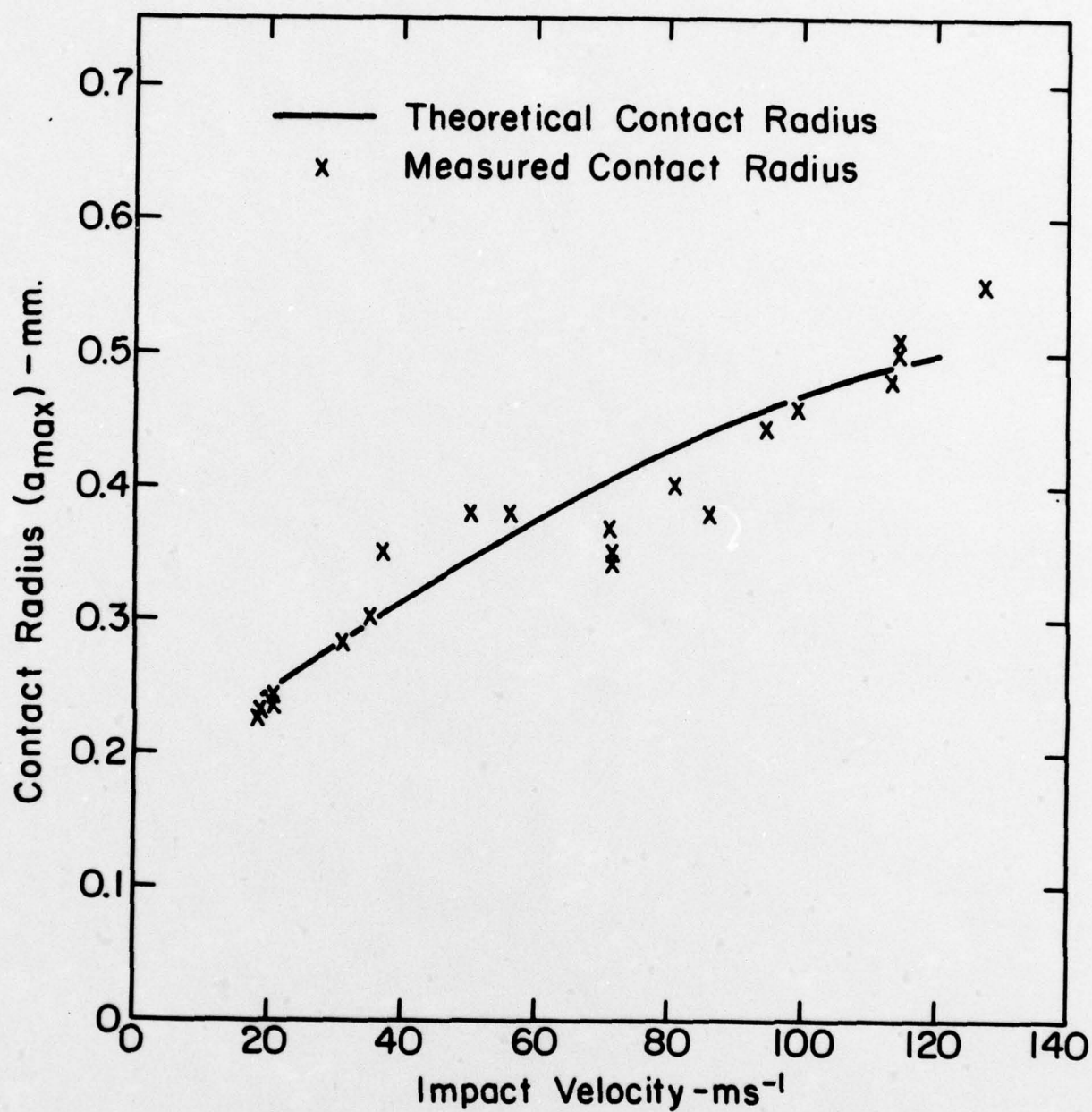


Figure 7 Contact Radius ( $a_{max}$ ) vs. Impact Velocity ( $V$ )

Values of  $P_{\max}$  were estimated by substituting the measured values of  $a_{\max}$  in Equation (1). These results are compared with theoretical values calculated using Equation (2), in Figure 8. The differences are similar to those in the previous figure. The inflection in the experimental data at velocities above  $40 \text{ ms}^{-1}$  coincides approximately with indentation of the surface, the onset of radial cracking and substantial branching of the ring crack, and may have been caused by one or more of these factors.

#### 5. Hertz cone lengths

Dimensionless load parameters<sup>(5)</sup> were calculated using values of  $P_{\max}$  calculated from some of the measured values of  $a_{\max}$  using Equation (1). The dimensionless load parameters and the measured values of  $a_{\max}$  were used to estimate the Hertz cone lengths (C) in the four cases in which sufficient data were available, using Figure 2 of the reference. The resulting values of C were 2-14 times the measured values. Strictly speaking, the theory does not apply in the present cases because  $a_{\max}$  is greater than  $r^*$  in every case except one in which a piece of debris on the glass surface was contacted by the sphere which induced the Hertz crack at much greater  $r^*$  than would normally be expected. However, continued increase in the load after crack formation might be expected to drive the crack deeper into the specimen than expected for cases in which  $a < r^*$ . This appears not to be the case. Part of the problem may be that there is insufficient time for the crack to propagate to the full extent expected at a particular load.

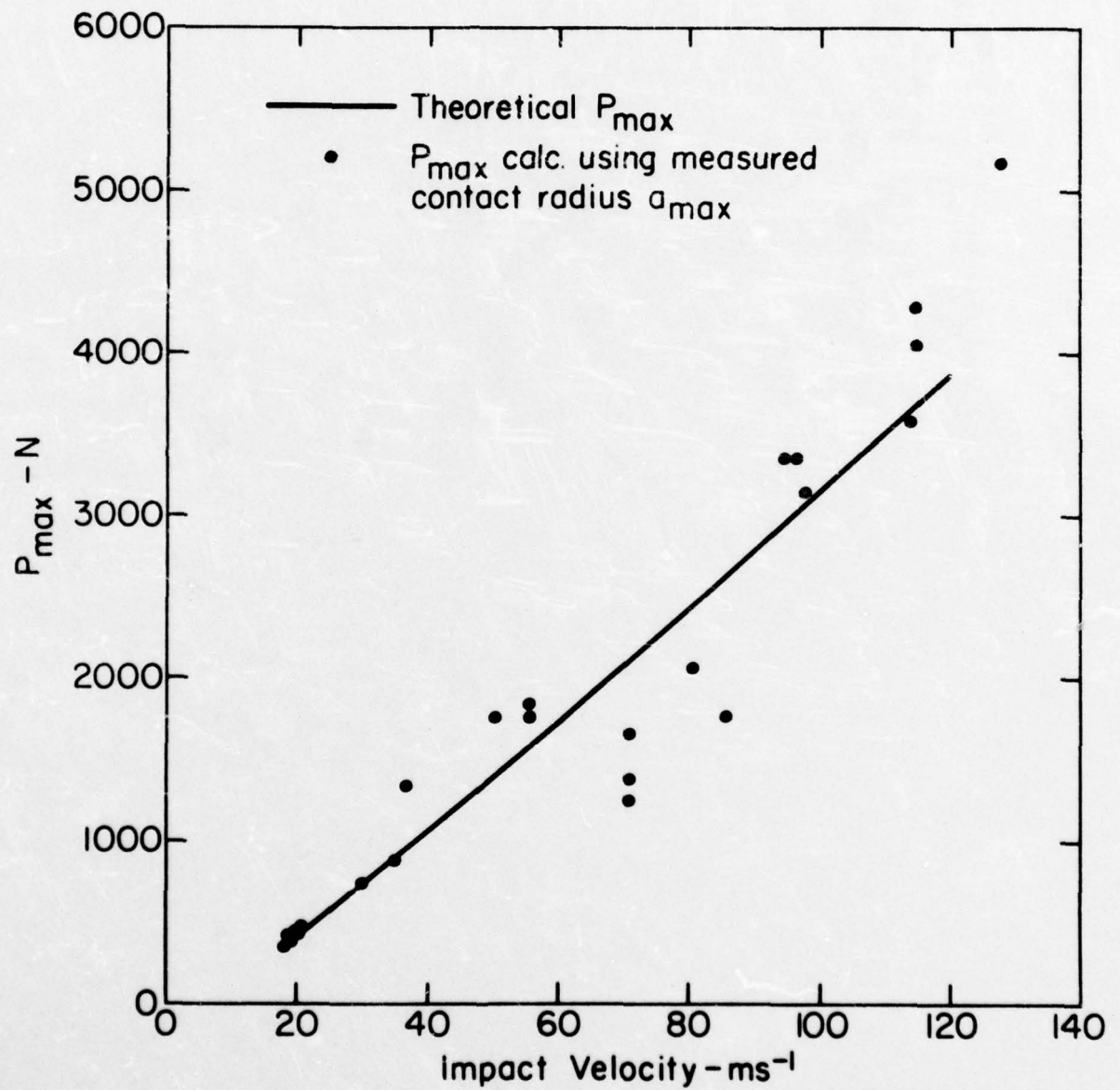


Figure 8 Maximum Impact Force vs. Impact Velocity



### III. LOCALIZED IMPACT DAMAGE IN GLASS AT ELEVATED TEMPERATURES

#### A. Procedures

Electric heaters were used to heat the glass plates to temperatures as high as 770°C. The arrangement of the heaters is illustrated in Figure 9. The temperatures at both faces of the glass plates were measured by the thermocouples. The voltages on the heaters were adjusted until the temperatures of both faces were equal. This condition was held for two minutes. Then, the heater on the front surface was removed and the gun was fired so that the specimen was impacted before substantial cooling could occur. The incoming and rebounding velocities were measured by high speed photography.

The impact damage was characterized by optical and scanning electron microscopy and by profilometry. Contact radii, indentation radii, radii of radial cracks, and coefficients of restitution were determined. These characteristics of the surface damage were compared with those observed at room temperature.

#### B. Results and Discussion

##### 1. Localized impact damage

After preliminary experiments in which indentations were observed at about 600°C, conditions were chosen for subsequent tests. One objective was to impact specimens having various viscosities ( $\eta$ ). In the following discussion, the results are presented in terms of temperature. To estimate the corresponding viscosities, a viscosity vs. temperature curve was constructed for the float glass by drawing a curve through one float glass

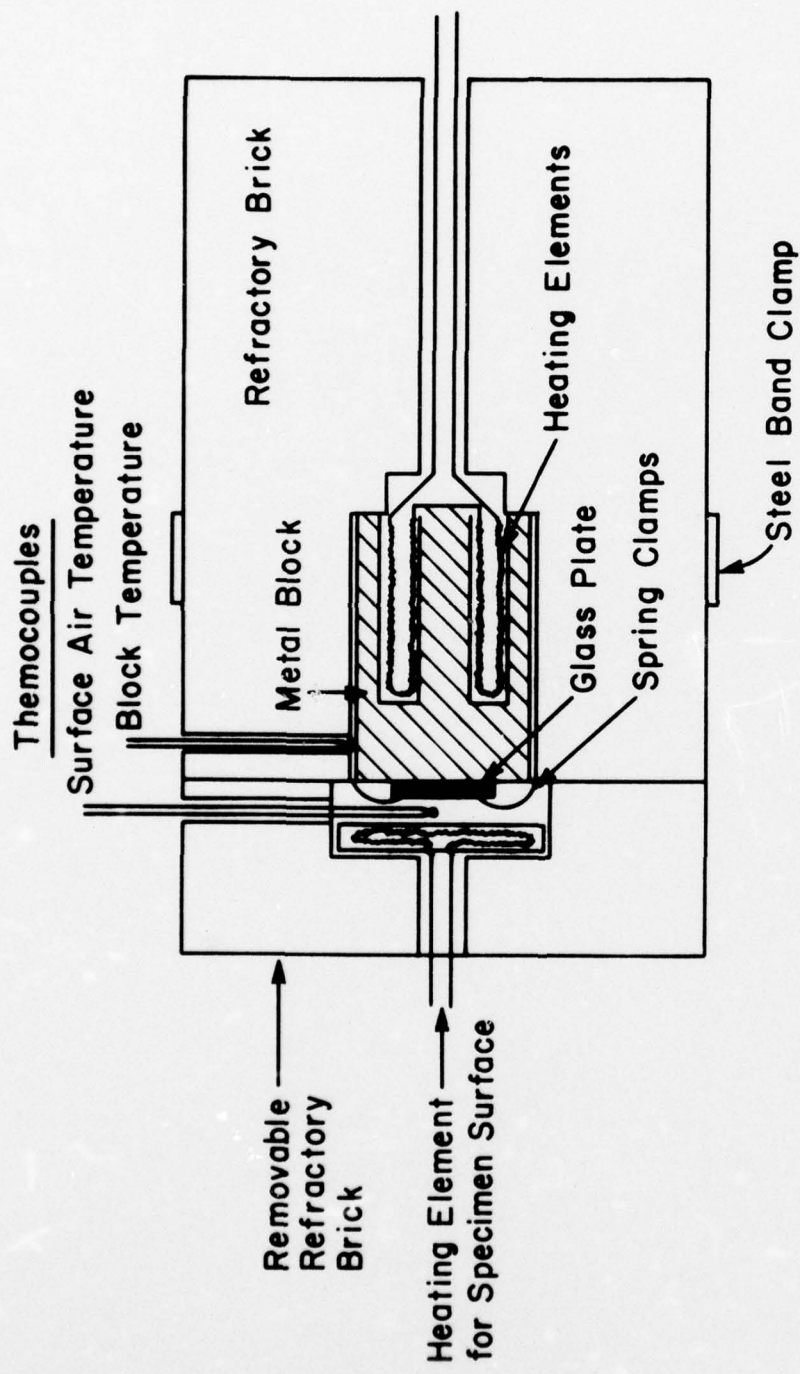


Figure 9 Experimental Arrangement Used to Heat Glass Plates for Elevated Temperature Impact Tests

data point parallel to a viscosity vs. temperature curve for another soda-lime glass<sup>\*</sup>. The results are given in Figure 10.

Specimens were impacted at various temperatures and velocities. In general, the extent of damage increased with increasing impact velocity as expected. Among the features observed were indentations, Hertz cracks, radial cracks, lateral vent cracks, and crushing. A schematic diagram of the variations in damage characteristics with temperature and velocity is given in Figure 11. The persistence of Hertz cracks at high temperatures was unexpected. Previous results<sup>(1)</sup>, based mainly on static indentation, led to the expectation of a transition from Hertz crack damage to indentation damage with increasing plasticity or decreasing viscosity. Another important observation is the decrease and eventual cessation of crushing with increasing temperature at high velocities.

The variation of the coefficient of restitution with both velocity and temperature is indicated for five different temperatures in Figure 12. It is evident that a change in physical response occurs in the temperature range between 525 and 650°C. At the lower temperatures the coefficient of restitution decreases at high velocities apparently because of extensive crushing. At higher temperatures the coefficient of restitution is never high because of indentation losses. However, the decrease at higher velocities is less than that of the lower temperature specimens apparently because there is substantially less crushing.

## 2. Determination of the indentation temperature at $50 \text{ ms}^{-1}$

The impact damage for specimens impacted at about  $50 \text{ ms}^{-1}$  and at various temperatures is illustrated in Figures 13 a-1. The photographs were taken with inclined illumination so that when the surface is indented the light

---

\* Kimble R-6.



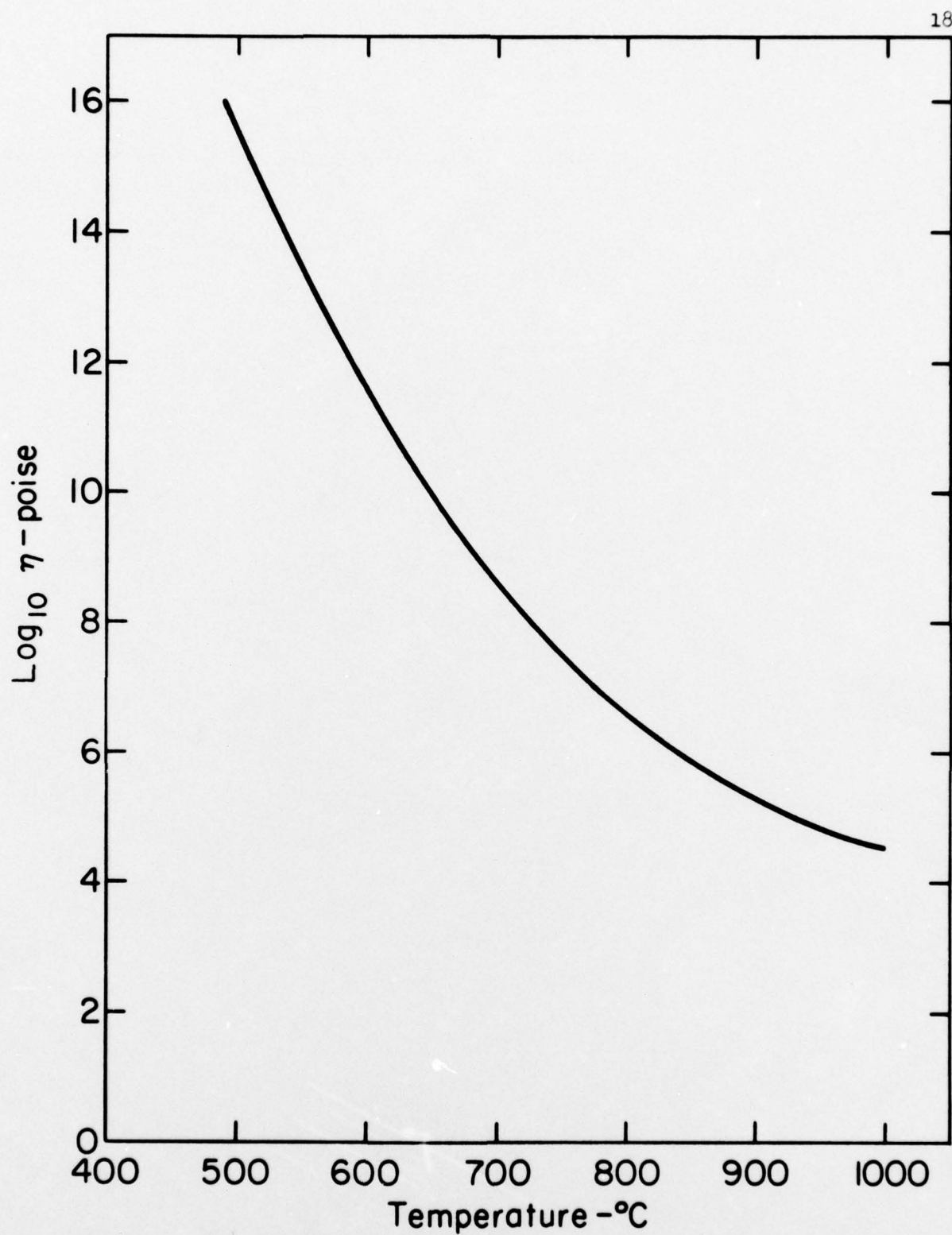


Figure 10 Estimated Log Viscosity vs. Temperature  
Curve for Float Glass

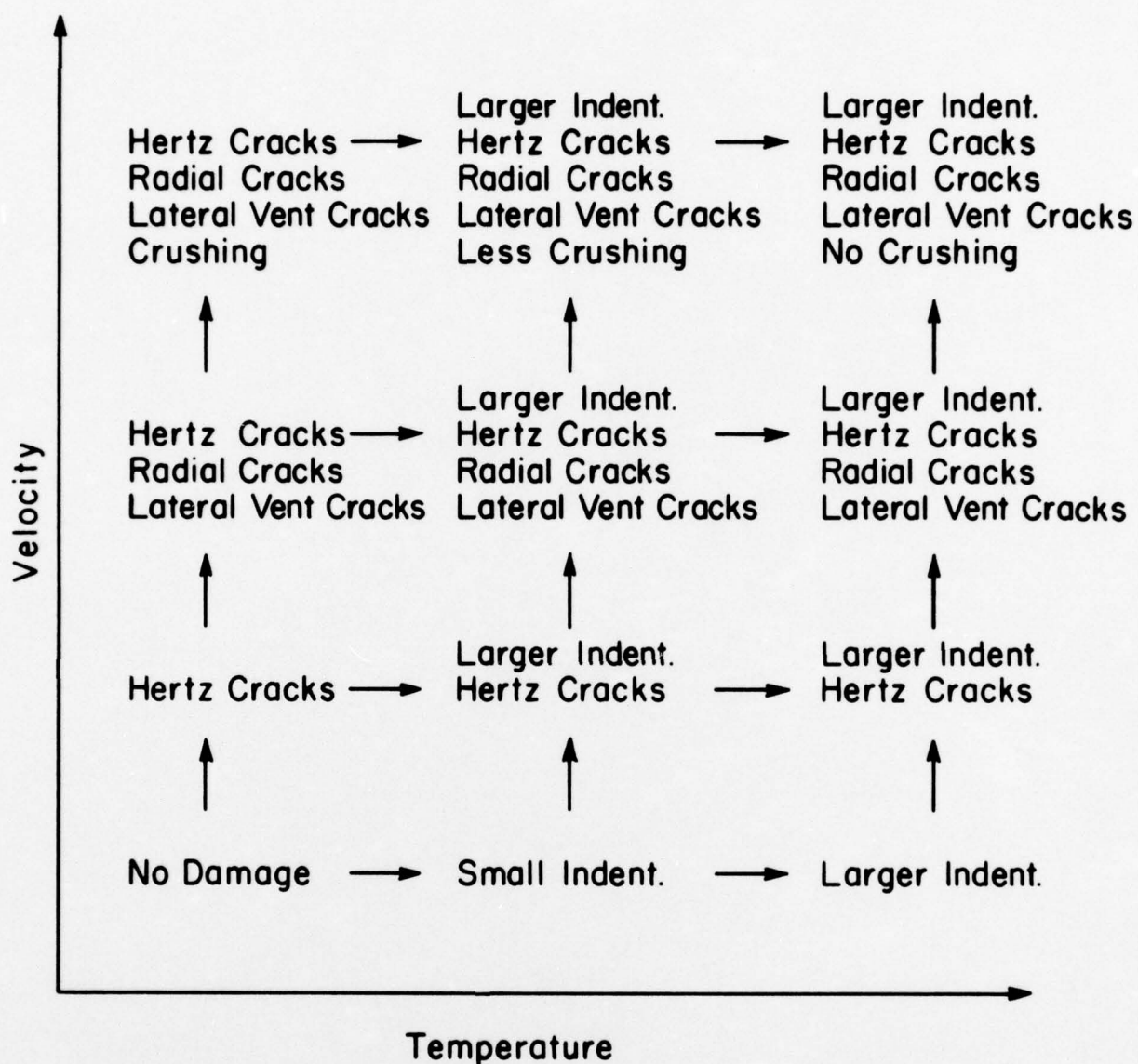


Figure II Schematic Representation of Damage Characteristics at Various Temperatures and Velocities

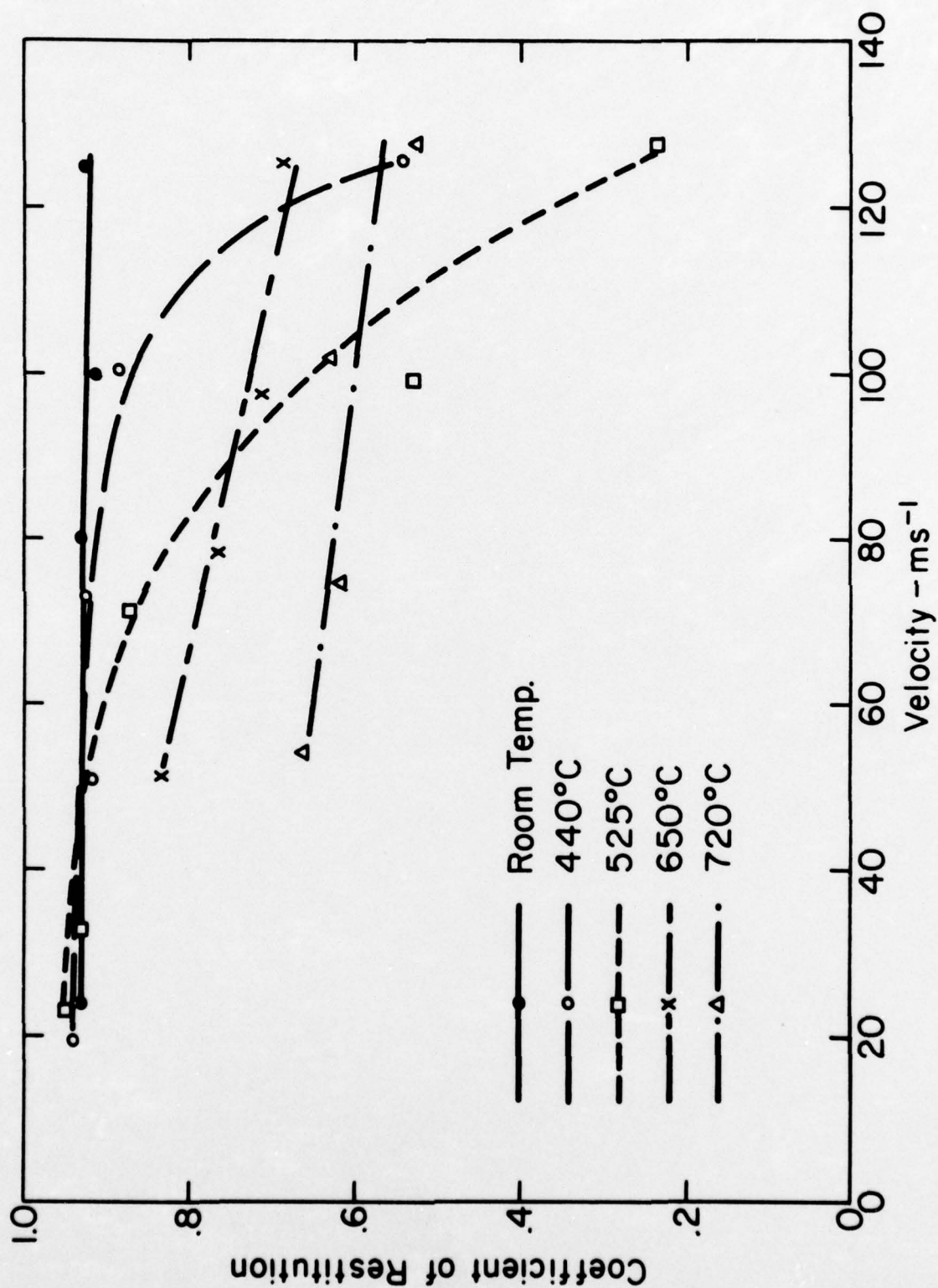


Figure 12 Coefficient of Restitution vs. Impact Velocity at Various Temperatures



is reflected from the near side (relative to the observer) and the far side appears dark. There is no definite evidence of indentation at temperatures up to about 525°C but above this temperature indentation occurred, the degree of indentation increasing with temperature.

The tendency toward radial crack formation increases with increasing indentation. The damage observed at 620 and 650°C is similar to that at 580°C except for greater indentation. At 683°C there are five cracks extending radially from the indentation. Two of these cracks are indicated by the dark "shadows" extending more or less horizontally from the indentation. The cracks do not extend to the surface and, in fact, they are contained within the cone crack. It seems likely that these cracks are median vent cracks as described by Lawn and Wilshaw<sup>(6)</sup>. Therefore, further indentation should be expected to extend these cracks to the surface to form radial cracks as shown at 700 and 720°C (these specimens were coated with a thin layer of gold, obscuring subsurface features). It should be noted that these cracks at 683°C are the only median vent cracks observed in this investigation.

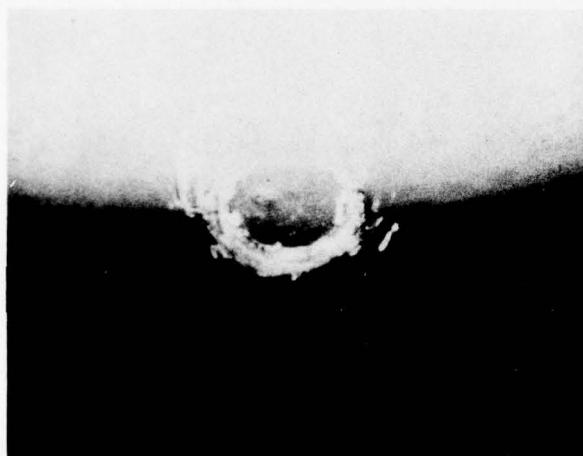
The coefficients of restitution of these specimens, at various temperatures, are plotted in Figure 14. There is an apparent discontinuity in the coefficient of restitution in the temperature range at which the indentations first occur. The kinetic energy of the incoming sphere is about 0.041 J. At lower temperatures the energy loss on impact is 0.0064 J (16%). At 580°C the energy loss on impact is 0.011 J (27%) indicating that the presence of observable indentations increases the kinetic energy loss by about 11%. Larger indentations result in greater losses.



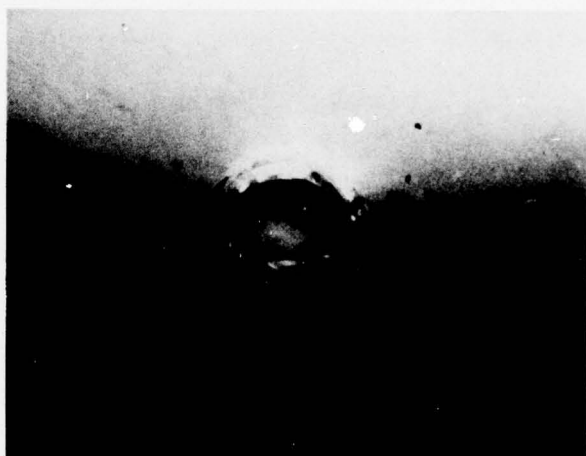
440°C



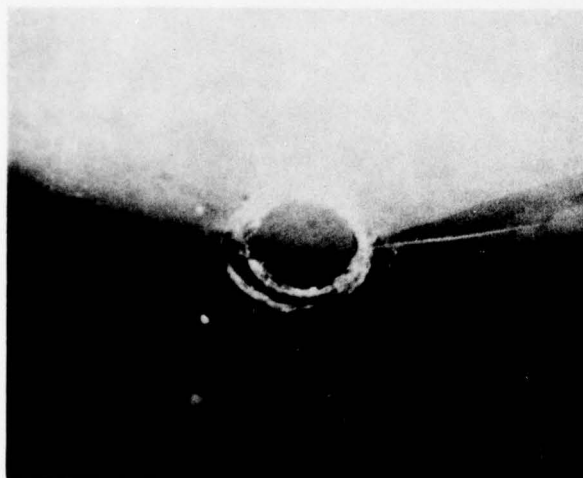
580°C



480°C



620°C



525°C

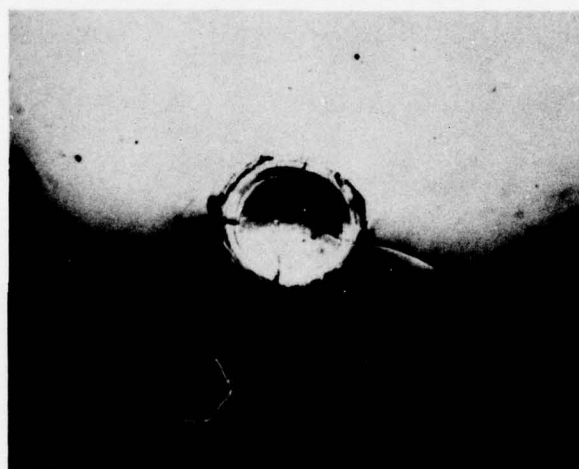


650°C

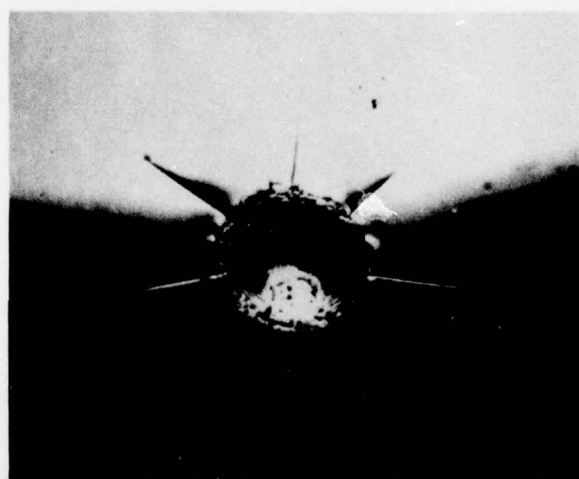
Figure 13 Indentations Observed at  $50\text{ms}^{-1}$  and Various Temperatures (27X)



683°C



700°C



720°C

Figure 13 Indentations Observed at  $50\text{ms}^{-1}$  and Various Temperatures



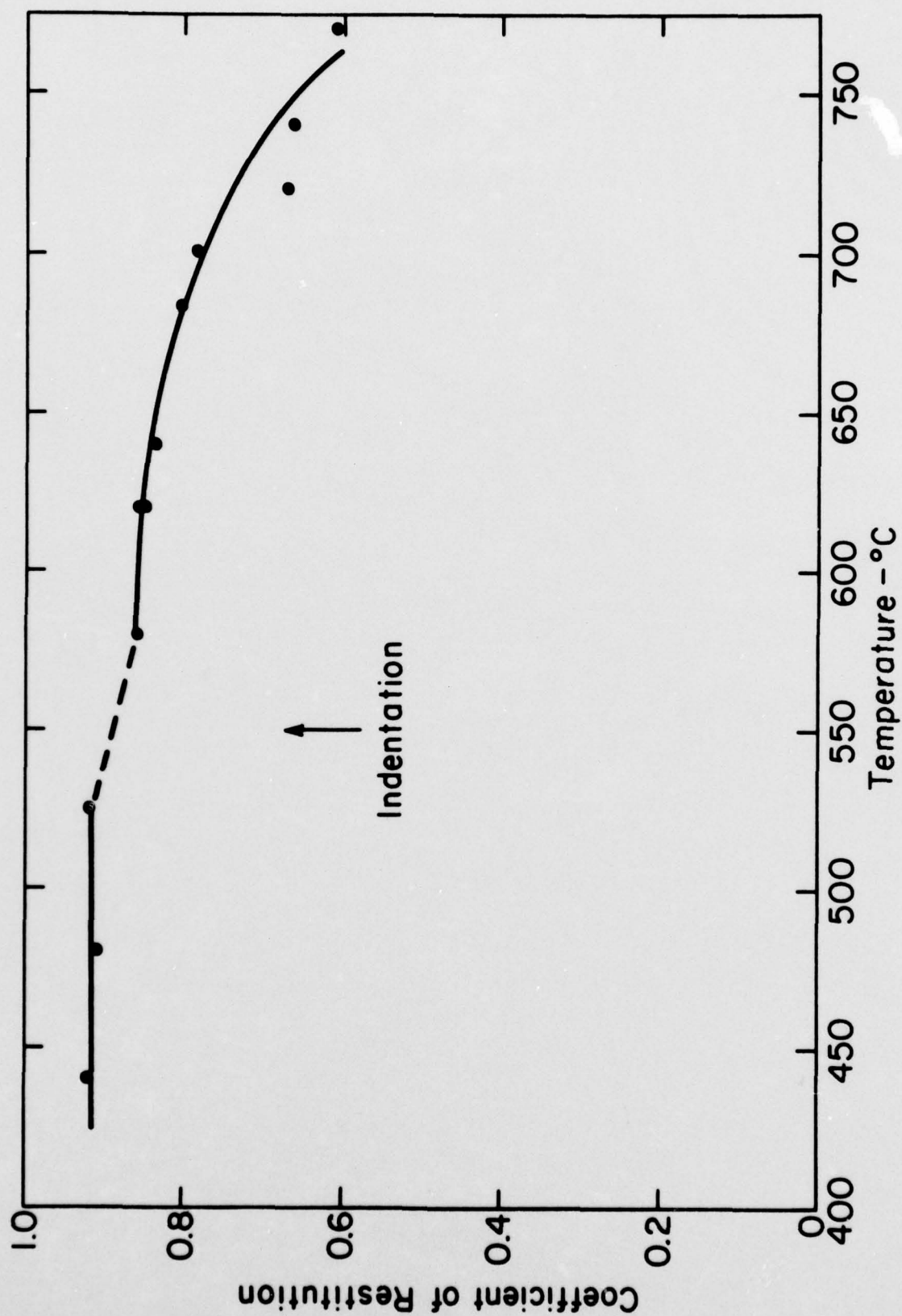


Figure 14 Coefficient of Restitution vs. Temperature for 3mm Diam. Glass Spheres Impacting Glass Plates at 50 ms<sup>-1</sup>

### 3. Impact damage at high temperatures and various velocities

Scanning electron micrographs of specimens impacted at various velocities and relatively high temperatures are presented in Figure 15. The photographs show increasing damage with increasing impact velocity as expected. The details of these observations are discussed in the following paragraphs.

The indentations are rather shallow as might be expected because the contact radii are so much smaller than the sphere radii. In one case (Specimen 121,  $V = 73.3 \text{ ms}^{-1}$ ,  $T = 700^\circ\text{C}$ ) the profiles of the indentation were determined at various distances from the center of the indentation using a profile measuring device. The results obtained for a profile near the center are illustrated in Figure 16. The vertical scale is 43 times the horizontal scale so that the indentation appears to be much deeper than it actually is. The profile shows that there is at least one circumferential crack in the indentation. There is a definite rim formed by material pushed up by the impact. The rim is raised about  $5 \mu\text{m}$  above the surrounding undisturbed material. The rim contains approximately three circumferential cracks, at least at the location of this particular contour. The indentation is about  $20 \mu\text{m}$  deep including the rim and is about  $800 \mu\text{m}$  in diameter.

There is a strong increase in the number of radial cracks with increasing impact velocity and temperature. One might expect the number of these cracks to be proportional to the total strain at the periphery of the indentation. Taking the circumference as proportional to the radius of the indentation ( $a$ ) and assuming that the stress varies as the velocity ( $V$ )



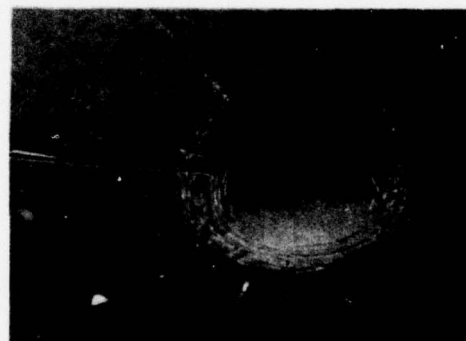
720°C 125 ms<sup>-1</sup>



720°C 102 ms<sup>-1</sup>



700°C 73 ms<sup>-1</sup>



720°C 74 ms<sup>-1</sup>

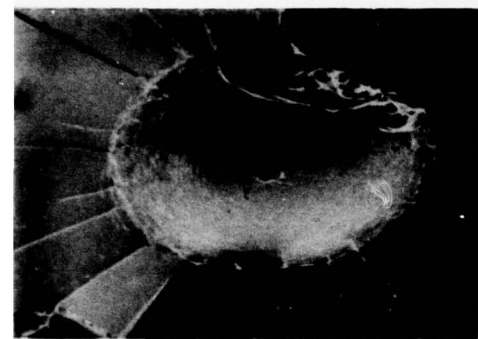


700°C 50 ms<sup>-1</sup>

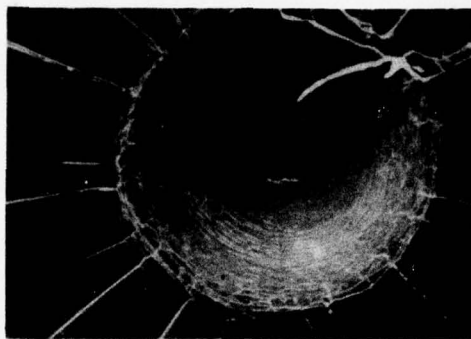


720°C 54 ms<sup>-1</sup>

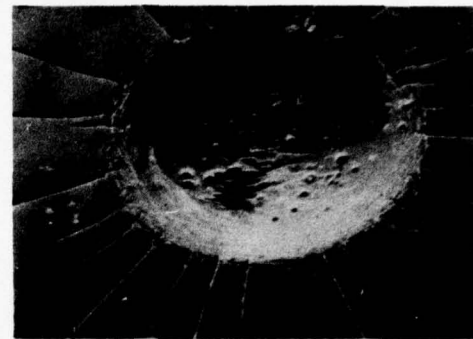




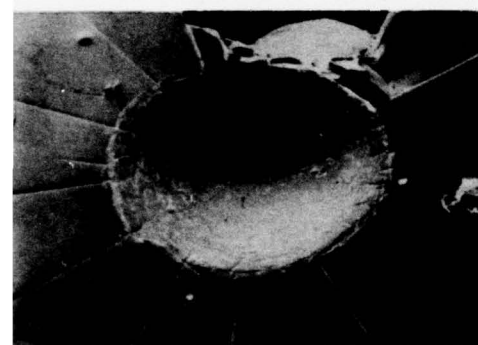
730°C 128ms<sup>-1</sup>



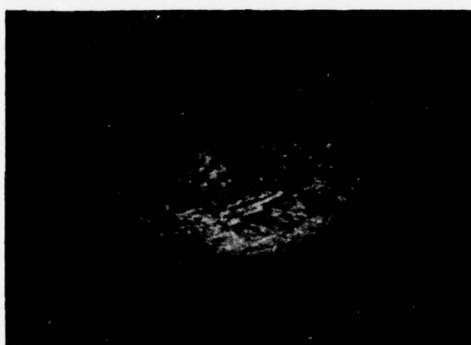
740°C 130ms<sup>-1</sup>



770°C 128ms<sup>-1</sup>



730°C 100ms<sup>-1</sup>



740°C 100ms<sup>-1</sup>



770°C 100ms<sup>-1</sup>

Figure 15 Impact Damage at High Temperature

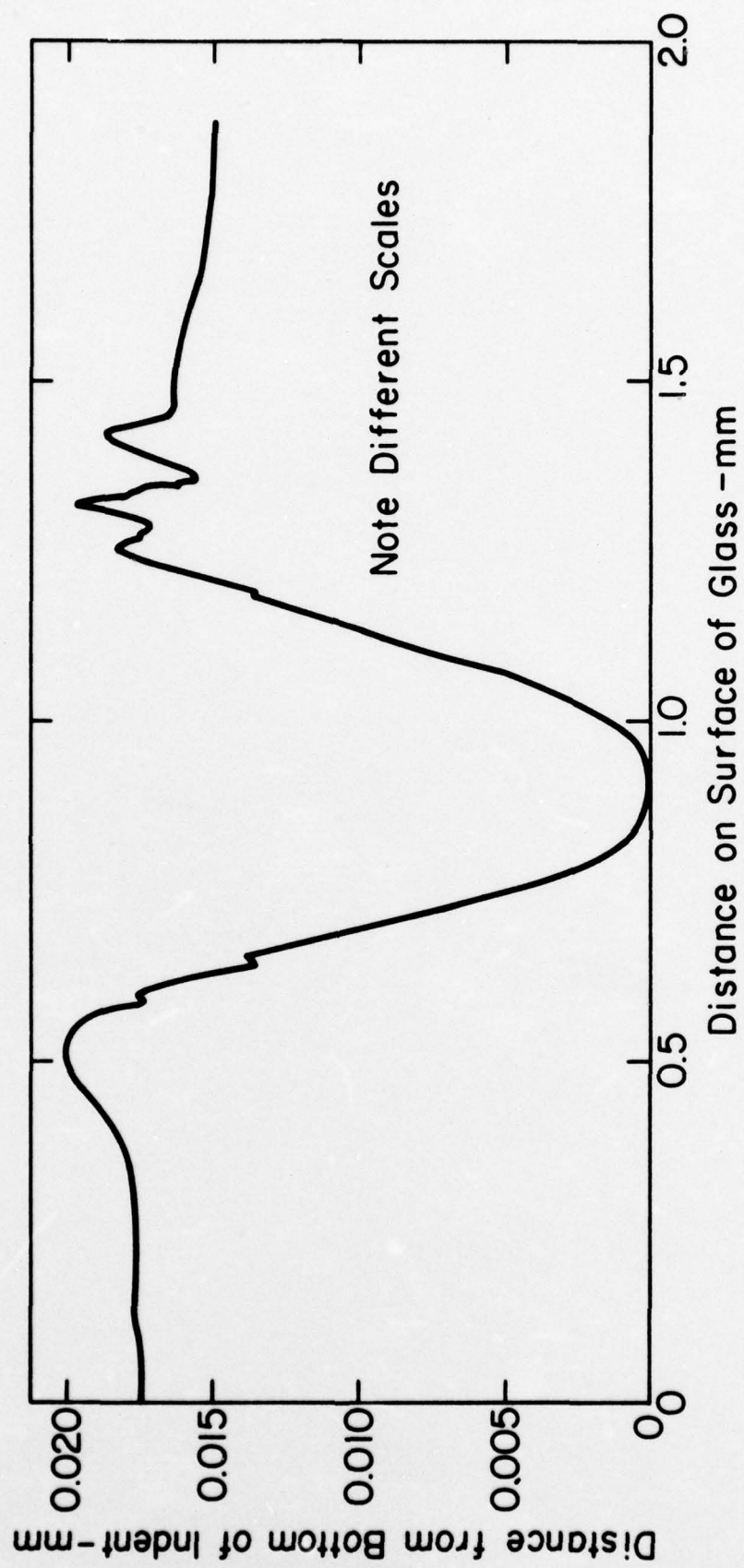


Figure 16 Profile of Indentation Formed by Impact at  $700^{\circ}\text{C}$  and  $74\text{ ms}^{-1}$   
(Specimen No. 121)

to the  $6/5$  power as it does for elastic impacts, the number of radial cracks was plotted versus  $aV^{6/5}$  in Figure 17. The essentially straight line is consistent with the above-stated expectation.

Attempts were made to correlate the radial crack lengths with various parameters reflecting the impact conditions. The variations in the radial crack lengths at individual impact sites and among the impact sites make it very difficult to decide which particular features are most significant. Therefore, we have not attempted to report these results.

Circumferential cracks were observed surrounding the impact sites. These cracks appear to be somewhat similar to the ring cracks formed at room temperature during static loading. The photograph of specimen 176 impacted at  $700^{\circ}\text{C}$  and  $50\text{ ms}^{-1}$  shows one or two of these circumferential cracks outside the indentation. With increasing velocity and temperature, the number of these cracks increases strongly. The locations of the cracks relative to the rim of the indentation also vary with temperature and velocity. In specimen 176, the first circumferential crack was formed just inside the rim; those last formed being on or just outside the rim. At higher velocities and temperatures a larger fraction of these cracks are inside the rim. It is interesting that the radius from the impact point to the first of these concentric cracks formed is practically constant for the conditions shown in Figure 15 except at the highest temperatures and velocities. This observation may indicate that these cracks tend to form at the same stress even though the impact conditions vary. The concentric cracks nearest the impact point appear to be short segments of cracks that have failed to link up. This observation may indicate that there is a high density of surface flaws, either preexisting or formed during the impact process.



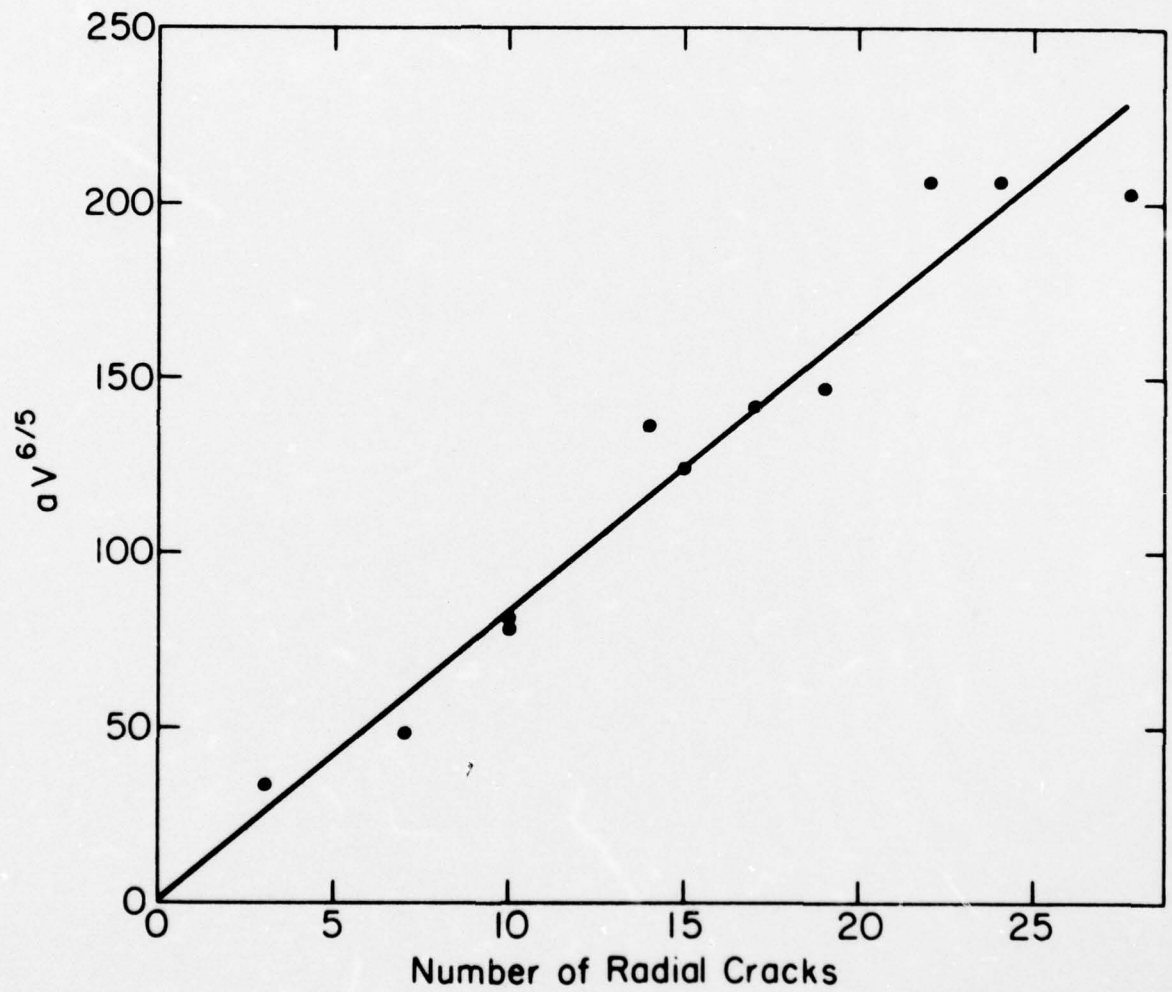


Figure 17  $aV^{6/5}$  vs. Number of Radial Cracks

The sub-surface damage is illustrated in Figure 18 for specimens impacted at high temperatures and relatively low velocities. Photographs of these specimens were chosen because the damage is less complex than in many other cases. The photograph of specimen no. 71 ( $740^{\circ}\text{C}$ ,  $51 \text{ ms}^{-1}$ ) is oriented so that light is reflected from three radial cracks rather than being transmitted through them to the camera. Therefore, these cracks appear dark. The contours are well defined, extending from the surface and ending at smooth curves. There is no indication of radial crack formation under the indentation. Therefore, these cracks do not form originally as median vent cracks and then extend to the surface.

Specimen 53 ( $770^{\circ}\text{C}$ ,  $57 \text{ ms}^{-1}$ ) shows similar radial crack formation. The interesting feature in this photograph is the Hertz cone crack which shows that, even in materials that deform rather readily ( $\eta \approx 10^7$  poise), cone cracks still form.

The tips of the radial cracks formed at high temperatures were examined in detail and were found to be close to elliptical as illustrated in Figure 19. The radii of the tips of cracks, formed at various temperatures and velocities were measured and are reported in Table I. The radii increase strongly with increasing temperature.

In some cases sharp cracks form which extend beyond the elliptical crack tips as shown in Figure 20. Formation of these cracks is puzzling. It may be that these cracks form under the influence of residual stresses after cooling to room temperature but the process by which these cracks form has not yet been observed. Strong birefringence was not observed at the crack tips.

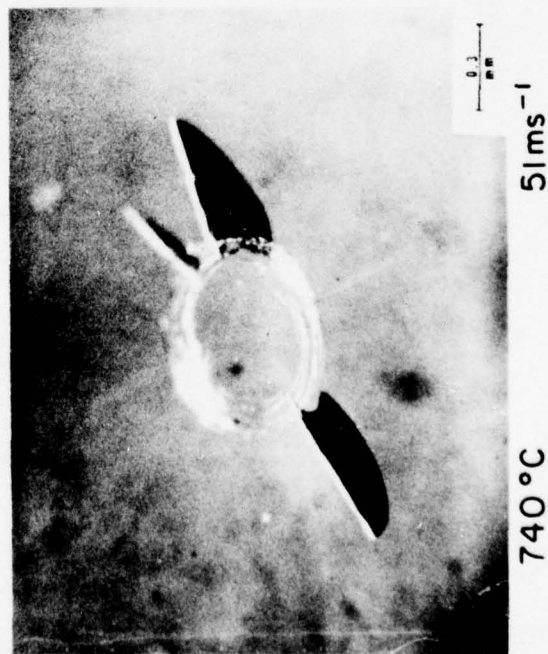
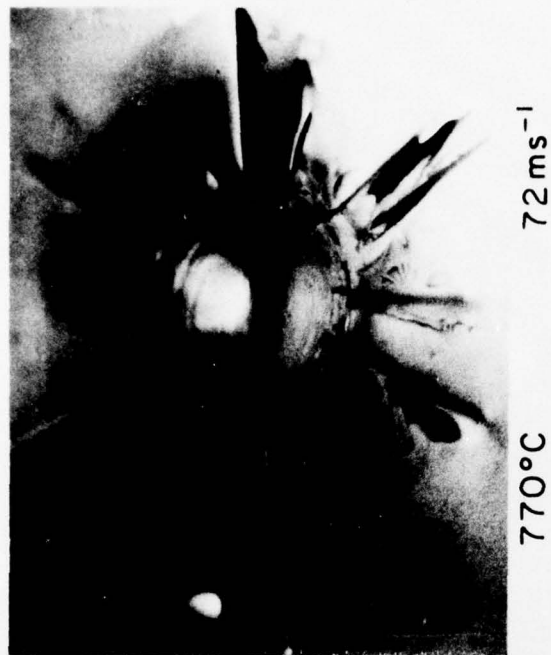


Figure 18 Radial Cracks at High Temperature (37X)

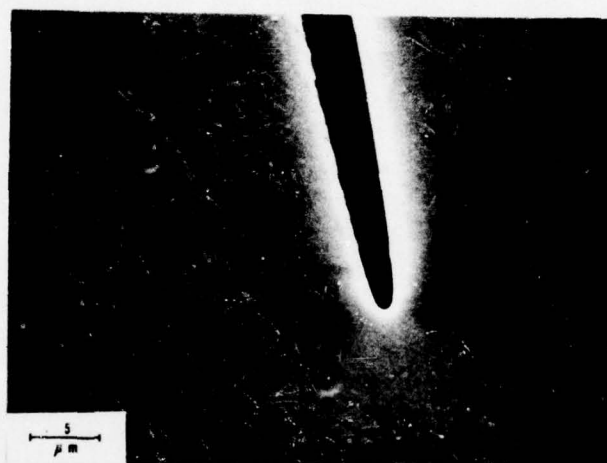


Figure 19 Radial Crack Tip ( $770^{\circ}\text{C}$ ,  $57\text{ ms}^{-1}$ )



Table I. Radial crack tip radii.

Temperature °C	700	720	740	770
Velocity ms <sup>-1</sup>	Crack Tip Radius μm			
~100	---	---	0.35-0.5	---
~ 75	---	---	0.3	0.5-0.55
~ 50	~ 0.1	0.25	0.35	0.6

At high temperatures and impact velocities, unusually large lateral vent cracks were observed as shown in Figure 21. Lateral vent cracks are believed to have an important role in material removal, for example, in grinding or sand blasting. Therefore, further investigation of conditions favorable to lateral vent crack formation might yield more efficient material removal processes.

#### IV. SUMMARY AND CONCLUSIONS

Localized impact damage in glass was investigated at temperatures from room temperature to 770°C and at velocities up to 138 ms<sup>-1</sup>. Several different types of impact damage were observed. In this section the variation of each type of damage with temperature and velocity will be described and compared.

It appears that a distinction should be made between indentations occurring at relatively low temperatures in the absence of viscous flow and indentations formed at relatively high temperatures (580°C and higher) as a result of viscous flow. At low temperatures the indentations are a



**Figure 20 Sharp Crack Extending from Elliptical Crack Tip (80X)**



**Figure 21 Lateral Vent Crack Formed at High Temperature (11X)**

secondary type of damage forming as a result of release of elastic stresses by other types of damage such as Hertz cracks, radial cracks, lateral vent cracks and crushing. At high temperatures at which indentations form as a result of viscous flow, the indentations are a primary type of damage. The diameters of these indentations increase with increasing impact velocity and temperature, as expected.

Hertz cracks form at impact sites both at low temperatures at which the response of the target is primarily elastic and at high temperatures ( $>525^{\circ}\text{C}$ ) at which the response is at least partly a result of viscous flow. Therefore, it is incorrect, for impacts of glass plates by glass spheres, to regard the damage mechanisms for cases in which indentation occurs as being completely different from those in which no indentation occurs. Viscous flow is a time consuming process. In the initial stages of impact the stress distributions may resemble those present during elastic impacts with radial tensile stresses and tangential compressive stresses. Hertz cracks may form during this stage. Later, as the indentation becomes deeper the tangential stresses may change sign leading to radial crack formation.

The number of radial cracks appears to be proportional to the total strain at the boundary of the indentation, as might be expected. The lengths of the radial cracks increase with increasing impact velocity but the data were not sufficient to determine the exact relationship between these variables.

The lateral vent cracks were formed after the radial cracks as indicated by the tendency to chip between the radial cracks. Enhanced lateral vent crack formation was observed at some elevated temperature

conditions. This observation might be of value for enhancing material removal rates during grinding or sand blasting.

The coefficients of restitution of impacts at room temperature decrease only slightly with increasing impact velocity. At intermediate temperatures, below those at which viscous flow results in indentations, the decrease in coefficient of restitution with increasing impact velocity is very great because of substantial crushing at the impact site. By contrast, at high temperatures indentation occurs at all velocities and the coefficient of restitution is never high.

The energy losses occurring during impact are determined by the change in velocity of the incoming and rebounding sphere and can be estimated by multiplying the mass of the sphere times the difference of the squares of these velocities. At room temperature the energy loss appears to increase linearly with the kinetic energy of the impacting sphere up to velocities at which radial cracks form ( $70 \text{ ms}^{-1}$ ). At higher velocities, the energy losses increase at greater than the linear rate.

#### REFERENCES

1. A. G. Evans, "Quasi-Static Solid Particle Damage in Brittle Materials," Rockwell International Science Center First Report, Contract N00014-75-C-0669 (February, 1976).
2. H. P. Kirchner and R. M. Gruver, "Localized Impact Damage in Ceramics," Ceramic Finishing Company Technical Report No. 4, Contract N00014-74-C-0241 (June, 1976).
3. S. Timoshenko and J. N. Goodier, "Theory of Elasticity," McGraw-Hill Book Co., New York (1951) p. 384.
4. W. Goldsmith, "Impact," Edward Arnold (Publishers) Ltd., London (1960) p. 266.



5. A. G. Evans, "Strength Degradation by Projectile Impacts," J. Amer. Ceram. Soc., 56 (8) 405-409 (August, 1973).
6. B. Lawn and R. Wilshaw, "Indentation Fracture, Principles and Applications," J. Mater. Sci., 10, 1049-1081 (1975).
7. A. G. Evans, M. E. Gulden, G. E. Eggum and M. Rosenblatt, "Impact Damage in Brittle Materials in the Plastic Response Regime," Rockwell International Science Center Technical Report SC5023.9TR, Contract N00014-75-C-0669 (October, 1976).

APPENDIX A  
LOCALIZED DAMAGE FROM NOMINALLY SIMILAR IMPACTS ON GLASS

Introduction

This research is an extension of earlier research in which penetration of surface damage caused by impacts of glass spheres on biaxially stressed glass plates was investigated<sup>(1)</sup>. Substantial variations in damage penetration and other characteristics for apparently similar impacts were observed. There was an obvious need to determine whether the variations arose as a result of variations in test procedures, variations in the specimens, or variations in the conditions surrounding the impact site. Therefore, variations of impact damage characteristics in a number of specimens subjected to similar impact conditions were investigated.

Procedures, Results and Discussion

The impact conditions chosen were conditions thought to be near the threshold at which impact damage occurs. The glass plates (79.4 mm diam x 6.35 mm thick) were subjected to a biaxial compressive surface stress of  $43 \text{ MNm}^{-2}$  by stressing them in flexure between two coaxial cylinders with radii of 15.5 and 33 mm. The plates were impacted by glass spheres, 3 mm diam, at a velocity of  $52 \text{ ms}^{-1}$ .

Forty specimens were tested with the following results.

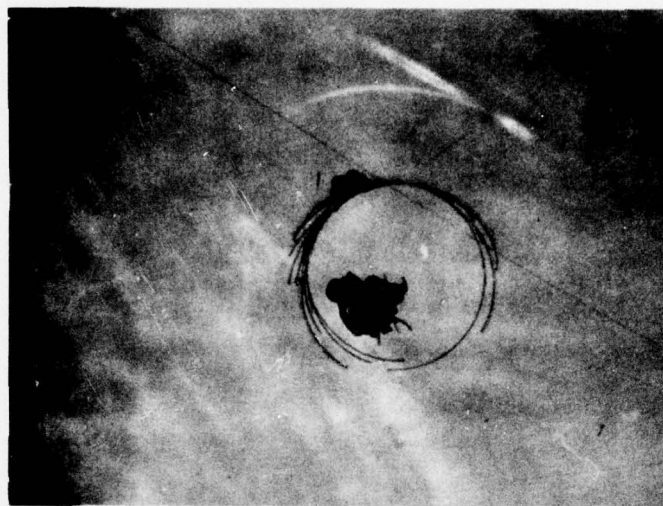
No surface damage	17 specimens
Hertz cone crack formation	17 specimens
Failure during loading (no impact)	4 specimens
Sphere fractured on impact	2 specimens
Total	<hr/> 40 specimens

Thus, the selected conditions were, in fact, near the threshold for Hertz crack formation and about half of the impacts resulted in Hertz crack formation.

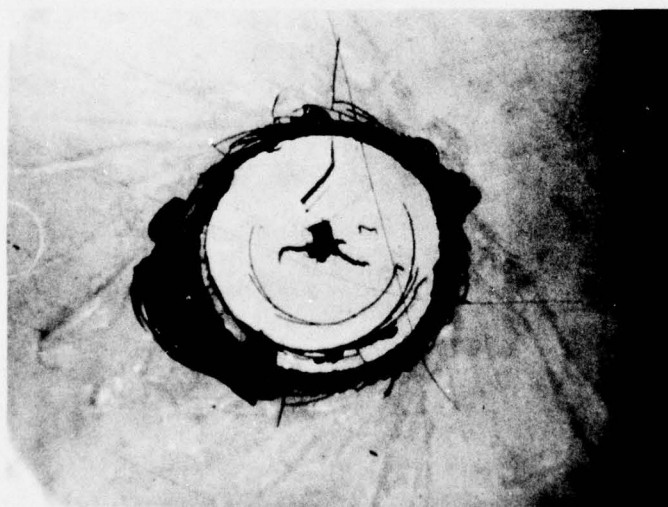
The Hertz cracks were variable in appearance. The most striking feature was the crack branching in the surface which occurred in every case. The clearest example is illustrated in Figure 1A. In at least four cases cracks formed which arrested leaving partial Hertz cracks. Completed cracks formed at larger radii in each of these cases. These features are illustrated in Figure 1B.

Frequently, the impact site is surrounded by an irregularly shaped crack as illustrated by the outer boundary in Figure 2A. This outer boundary is the intersection of a crack extending from the "ring" crack and partly down the cone, with the surface. In some cases the glass in this space between the cone crack and the surface pops out during the impact. Radial cracks sometimes form in the glass in this space as shown in Figure 2B. The radial cracks appear to decrease the radius to the outer boundary.

The observed variability is not mainly the result of variations in sphere velocity. Ballistic pendulum tests at the particular chamber pressure yielded velocities ranging from 51 to 53 ms<sup>-1</sup>. Furthermore, the contact radii



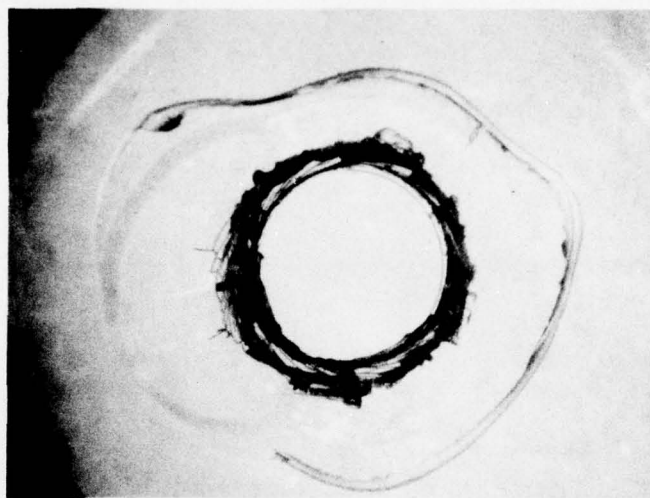
A. Hertz Crack Showing Branching



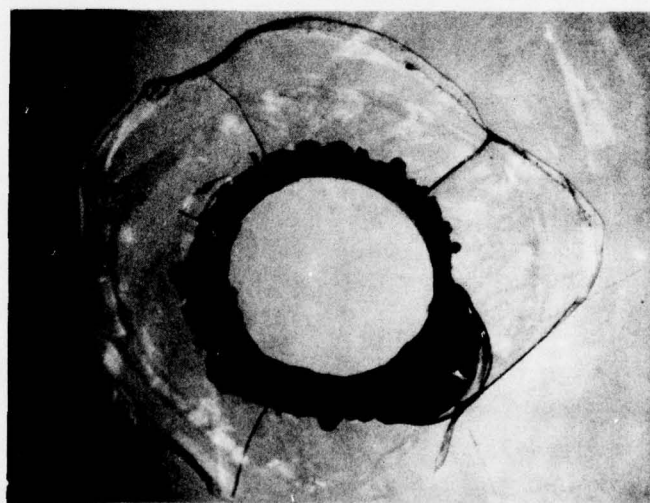
B. Partial Hertz Crack Inside a Completed Spiral Crack

Figure 1 Characteristics of Surface Cracks (42.5X)





**A. Unsymmetrical Crack Intersection with Surface**



**B. Radial Cracks**

**Figure 2 Intersections of Cracks with Surface (42.5X)**

( $a_{\max}$ ) were remarkably uniform averaging 0.391 mm with a standard deviation of 0.0045 for the specimens forming Hertz cracks and 0.389 mm with a standard deviation of 0.018 for specimens not forming Hertz cracks. Therefore, it seems reasonable to conclude that most of the observed variability resulted from variations in size, orientation and distribution of the surface flaws.

The Hertz crack radii ( $r^*$ ), crack depths ( $L$ ) and cone angles ( $\alpha$ ) of the specimens forming Hertz cracks are given in Table I. In each case two values of  $r^*$  were measured,  $r^*_{\min}$  measured to the innermost damage and  $r^*_{\max}$  measured to the outermost damage. Small Hertz crack radii appear to be associated with small crack depths but at large radii, the crack depths were extremely variable.

Further analysis is handicapped by the fact that in these impact tests there is no direct evidence of the value of ( $a$ ) when the fracture originates. In static tests the values of  $r^*/a$  range from one to two becoming closer to one with increasing indenter radius<sup>(2)</sup>. In order to use the elastic theory to estimate the stresses at which the cracks form, it is necessary to assume values of  $r^*/a$ . Based on the fact that the cracks extend to about  $r^*_{\max}/a_{\max}$  values of 1.36, it is reasonable to consider this as a maximum value. On the other hand, values of  $r^*_{\max}/a_{\max}$  less than one were observed in two cases. It is not at all obvious why these particular cracks did not continue to propagate. In any case, based on this evidence it was decided to calculate fracture stresses assuming  $r^*/a = 1.2$  when fracture originated.

The equation used to calculate the radial stress ( $\sigma_{11}$ ) was<sup>(3)</sup>

$$\sigma_{11} = \frac{(1 - 2\nu)P}{2\pi a^2} \quad (1)$$

Table I. Characteristics of Hertz cracks formed by similar impacts of glass spheres on glass plates.  
(Impact velocity  $52 \text{ ms}^{-1}$ , applied compressive stress  $43 \text{ MNm}^{-2}$ )

Specimen Number	Hertz Crack Radius-mm * $r_{\text{max}}$ $r_{\text{min}}$		Penetration (L) mm	Cone Angle ( $\alpha$ ) Degrees	Comments
1	0.470	0.323	0.48	22-25	Branched cracks with radial cracks
3	0.447	0.306	0.65	21	Branched cracks
4	0.447	0.341	0.1, 0.25	15-22	Branched cracks
5	0.500	0.365	0.352	22	Branched cracks
6	0.447	0.235	0.365	18	Inner partial, outer branched crack
9	0.470	0.259	0.45, 0.56	24	Inner and outer spirals
10	0.459	0.247	0.43	19, 25	Inner and outer spirals
12	0.353	0.176	0.09	18	Inner partial, outer branched crack
14	0.471	0.247	0.22, 0.27	15, 20	Inner partial, outer spiral
18	0.447	0.341	0.345	18, 23	Branched cracks
21	0.459	0.376	0.26	16, 20	Circular branched crack
25	0.471	0.235	0.43	25	Inner partial, outer spirals
29	0.518	0.365	0.34, 0.43	18-22	Branched cracks
31	0.353	0.282	0.07	?	Just completed, branched cracks
32	0.435	0.306	0.30, 0.40	17, 23	Branched cracks with one radial crack
38	---	0.294	0.45, 0.55	18-24, 26	Hemitoroid ejected
39	0.529	0.353	0.40	18, 18-22	Branched cracks

in which  $P$  is the impact force given by Equation (1) of Section II. The calculated fracture stress for the fracture originating at the smallest value of (a) (specimen 12) was  $275 \text{ MNm}^{-2}$ . For specimen 31 the calculated fracture stress was  $441 \text{ MNm}^{-2}$ . A method for experimentally estimating the fracture stresses of Hertz cracks using the radius at crack branching is described in Appendix B. This method was used to estimate the fracture stress of specimen 31. The radius at crack branching was approximately  $47 \text{ }\mu\text{m}$  yielding a fracture stress of  $365 \text{ MNm}^{-2}$ . To be comparable with the previous calculation, the applied flexural stress of  $43 \text{ MNm}^{-2}$  must be added to the value yielding  $408 \text{ MNm}^{-2}$ . In view of the assumptions and uncertainties in the methods, the agreement between the calculated and experimental values, 441 and  $408 \text{ MNm}^{-2}$  respectively, is remarkable. Using the method of Krohn and Hasselman<sup>(4)</sup> the flaw size necessary to cause crack branching at a particular radius is 1/10th the radius yielding an estimated flaw size of  $4.7 \text{ }\mu\text{m}$ . It should be noted that this estimate assumes that the flaw is oriented perpendicular to the radial stress. This flaw size can be compared with flaw sizes of about  $30 \text{ }\mu\text{m}$  observed by Langitan and Lawn<sup>(5)</sup> for glass abraded by No. 240 SiC powder. The calculated fracture stress for the specimen with the largest  $r_{\text{min}}^*$  (specimen 21) was  $588 \text{ MNm}^{-2}$ .

Assuming that fracture stress varies inversely as the square root of the flaw size and that the above estimate of  $4.7 \text{ }\mu\text{m}$  is correct for the flaw size of a specimen fracturing at  $441 \text{ MNm}^{-2}$ , the range of flaw size necessary to account for this range of fracture stresses is 2.6 to  $12 \text{ }\mu\text{m}$ .



### Conclusions

In 40 uniformly abraded specimens subjected to similar impacts near the threshold for Hertz crack formation, substantial variations in impact damage were observed. Hertz cracks were formed in about half of the specimens and ranged in depth from 70-650  $\mu\text{m}$ . The variabilities of the impact velocity and contact radii were small. Therefore, the variability in the damage is attributable to variations in the size, orientation and distribution of the surface flaws, despite the efforts made to obtain a dense, uniform distribution of flaws.

In a particular case the fracture stress, for Hertz crack formation, was calculated from the radius at branching of the ring crack. This fracture stress,  $408 \text{ MNm}^{-2}$ , was close to the stress expected at the fracture origin as calculated from the Hertzian stress distribution. The flaw size at the origin of the Hertz crack was calculated using the method of Krohn and Hasselman<sup>(4)</sup> and found to be 4.7  $\mu\text{m}$ .

### References

1. H. P. Kirchner and R. M. Gruver, "Localized Impact Damage in Glass," Ceramic Finishing Company Technical Report No. 4, Contract N00014-74-C-0241 (June, 1976).
2. T. R. Wilshaw, "The Hertzian Fracture Test," J. Phys. D: Appl. Phys. 4, 1567-1581 (1971).
3. B. R. Lawn and T. R. Wilshaw, "Fracture of Brittle Solids," Cambridge University Press, New York (1975) p. 20.
4. D. A. Krohn and D. P. H. Hasselman, "Relations of Flaw Size to Mirror in the Fracture of Glass," J. Amer. Ceram. Soc. 54(8) 411-(1971).
5. F. B. Langitan and B. R. Lawn, "Hertzian Fracture Experiments on Abraded Glass as Definitive Evidence for an Energy Balance Explanation of Auerbach's Law," J. Appl. Phys. 40(10) 4009-4017 (September, 1969).

## APPENDIX B

## BRANCHING OF HERTZ CRACKS

H. P. Kirchner and R. M. Gruver<sup>1</sup>Introduction

Impact by blunt, for example spherical, objects may cause Hertz cone crack formation in brittle materials (Figure 1). The cone cracks are similar in some respects to those formed by "static" indentations<sup>(1)</sup> but there are significant differences. For example, the relative absence of sub-critical crack growth during impact leads to fractures at higher stresses and the expectation that crack branching will have a larger role in the fracture process. Crack branching of Hertz cracks in the impact surface is described in this paper. Branching of the main cone crack was reported previously<sup>(2)</sup>.

Procedures, Results and Discussion

Soda-lime glass plates (6.35 mm thick and 79 mm diam) were lightly abraded, stressed biaxially in flexure between concentric cylinders (diameters 15.3 and 33 mm) and impacted at various velocities on either the compressive or tensile surfaces by glass spheres (1.5 mm radius). The biaxial stresses were low relative to the impact stresses and were applied as part of a study of the effect of stress on penetration of surface damage and remaining strength which has been reported separately<sup>(2)</sup>. These stresses are not considered further in this paper. For most of the present specimens, conditions were chosen so that a minimum amount

---

<sup>1</sup>Ceramic Finishing Company, State College, Pennsylvania, U.S.A.

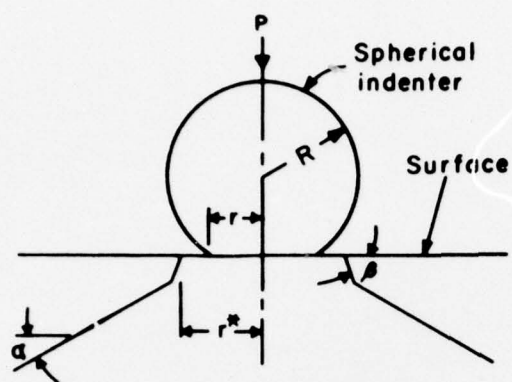


Figure 1 Hertz Crack

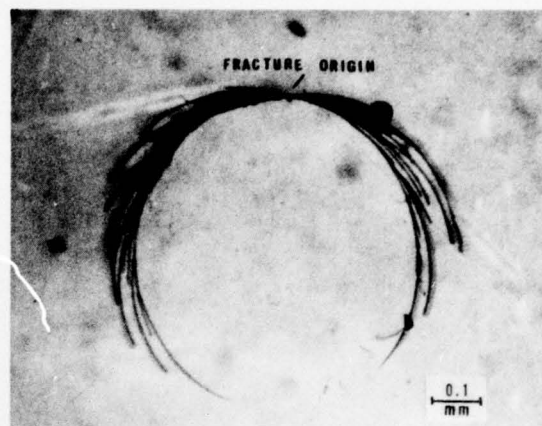


Figure 2 Partial Hertz Crack

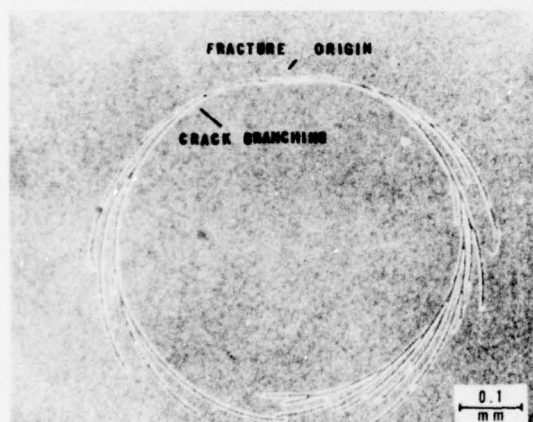


Figure 3 Complete Hertz Crack

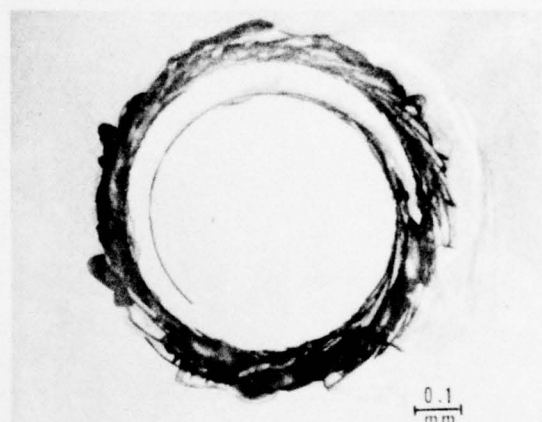


Figure 4 Spiral Hertz Crack

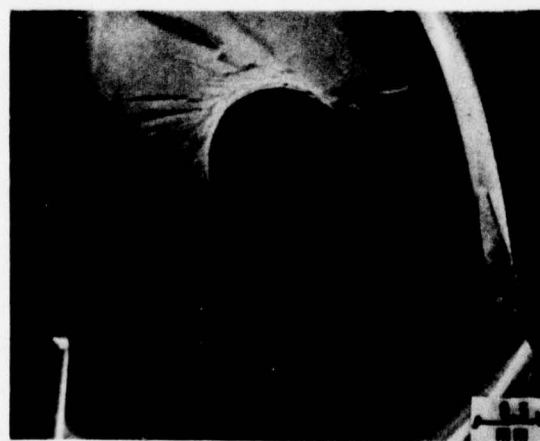


Figure 5 Hackle on the Surface of the Cone Crack

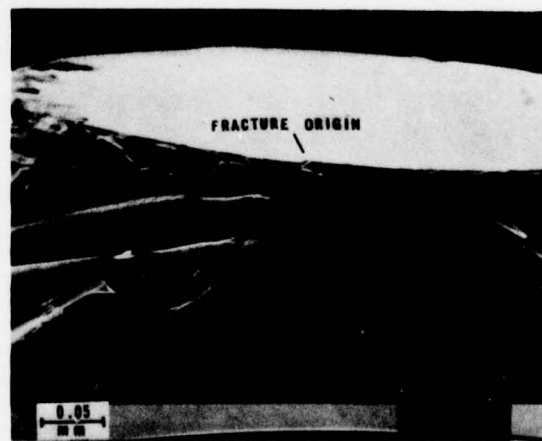


Figure 6 Side View of Hertz Cone

of surface damage was observed. This was done in order to have the simplest features available for characterization and analysis. Before impact, the impact surfaces were coated with a thin layer of soot. After impact the contact radius ( $r_{\max}$ ) was measured from the impression in the soot. Then, the soot was removed and the Hertz crack radius ( $r^*$ ) was measured. The fracture surfaces were characterized by optical and scanning electron microscopy. Etching with hydrofluoric acid was used to bring out the fracture features.

Usually, Hertz cracks at surfaces have been described as a single circular crack or as concentric cracks. The crack patterns observed in the present investigation were much more complex and variable than would have been expected based upon these previous descriptions. The surfaces, prior to etching, show cracks with very ragged appearances. Etching reveals that the underlying cracks have much smoother contours (Figures 2-4). Apparently, at some stage during the impact cycle the forces transmitted across the cracks cause extensive formation of thin chips. Etching removes these chips revealing the underlying smooth curves.

The Hertz cracks may be partial cracks (Figure 2), completed cracks (Figure 3) or spirals (Figure 4). In Figure 2, the fracture origin is at the narrow portion of the crack pattern at the top of the photo. This fact has been confirmed. For example, hackle are observed in the surfaces of the cone cracks as shown in Figure 5. The fracture origins are located at the intersections of the hackle. Figure 2 also shows extensive crack branching. Figure 3 illustrates a just completed Hertz crack with the fracture origin at the top of the photo and extensive crack branching. In this case, the width of the crack ( $r^*$ ), measured horizontally across the surface, is much greater than the height. This observation suggests that



the portion of the crack shown in the top half of the photo formed during the first half of the impact cycle as the circle of maximum tensile (radial) stress expanded, and the lower half formed during the second half of the impact cycle as it contracted. In some cases, one side of the Hertz crack arrests while the other side continues to propagate. In these cases, spirals are formed as indicated in Figure 4. The outer portion of these spirals always appears to be a complex mass of cracks. Apparently, crack branching occurs during the first half of the cycle and continues during the contraction of the circle of maximum stress leading to the thick outer ring of cracks.

Confirmation of the normal sequence of fracture features is shown in Figure 6 which is a side view of the Hertz cone in which the fracture origin, mirror, mist and hackle are indicated.

For a particular material and set of test conditions, crack branching occurs at a constant value of stress intensity factor ( $K_B$ ) as expressed by the following relation<sup>(3)</sup>

$$K_B = Y_B \sigma_f a_B^{1/2} \quad (1)$$

in which  $\sigma_f$  is the fracture stress,  $a_B$  is the crack radius at crack branching and  $Y_B$  is the geometrical factor appropriate for the crack at branching. In the present work, the mirror is considered to include the mist so that the fracture mirror radius and  $a_B$  are equivalent.  $K_B$  has been determined in tension and in flexure for numerous ceramics and glasses and several applications of this information have been demonstrated<sup>(3-7)</sup>.

A strong correlation between  $K_B$  and Young's modulus ( $E$ ) was observed<sup>(7)</sup> and used to suggest a strain intensity criterion for crack branching which permits prediction of  $K_B$  for various materials<sup>(8)</sup>.

Hertz cracks originate at or very near the surface where the flaws are subjected to biaxial stresses. The radial stress ( $\sigma_{11}$ ) is tensile and ideally at the contact radius has a magnitude of  $0.261^*$  times the average pressure ( $p_0$ ) at the impact site. For ideal elastic impact the tangential stress is compressive at the surface. However, as shown by Evans et al<sup>(9)</sup>, inelastic deformation at the impact site changes the tangential stress to tensile.

The radii at crack branching and Equation 1 can be used to estimate the stresses at which the Hertz cracks form. To do this it is necessary to assume that the crack branching is adequately treated by considering only the principal tensile stress. Further, it is necessary to choose an appropriate geometrical factor  $Y_B$ . The portion of the Hertz crack nearest the surface extends about 50  $\mu\text{m}$  into the specimen before flaring out to form the main cone. As long as the flaw size and the radius at crack branching are small relative to the depth of this portion of the crack and the contact diameter, it seems best to consider that the present case is approximated by a surface flaw loaded in tension, in which case  $Y_B$  should be 1.12. However, near the surface the Hertz crack is not quite perpendicular to the surface. The effect of this inclination to the surface has not yet been investigated.

---

\* Assuming Poisson's ratio of the glass is 0.239.

Two methods are available for measuring the crack radius at crack branching. One can locate the fracture origin in the impact surface as indicated in Figure 3 and measure the distance from the fracture origin to the first branch. Alternatively, one can project the hackle on both sides of the mirror to the surface as in Figure 6. Presumably, the fracture origin is located midway between the intersections of the hackle with the surface. A possible flaw, approximately at this location, is indicated in the figure. The radius at crack branching ( $a_B$ ) is one half of the distance between the intersections of the hackle with the surface. There are numerous complications in making these measurements. A particular problem is that chipping frequently occurs near the fracture origin, obscuring needed features.

$K_B$  has been determined for soda-lime and similar glasses in many experiments<sup>(3,5,10)</sup>. A representative value for soda lime glass is  $2.8 \text{ MPa} \cdot \text{m}^{1/2}$ . Fracture stresses were estimated by substituting for  $a_B$  and  $K_B$  in Equation (1) with the results shown in Table I. The estimated stresses ranged from 228 to 559 MPa. Values of the ideal elastic stresses at the contact radius were calculated using<sup>(11)</sup>

$$\sigma_{11} = \frac{(1 - 2\nu)P}{2\pi r^2} \quad (2)$$

in which  $\nu$  is Poisson's ratio and the load  $P$  is given by<sup>(12)</sup>

$$P = \frac{3E_1 r^3}{4CR} \quad (3)$$



in which  $E_1$  is the Young's modulus of the glass plates ( $6.9 \times 10^{10}$  Pa),  $C$  is a factor taking account of the elastic properties of the projectile and target with a value of 1.06. The calculations using Equation 2 were based on the assumption that the fracture initiated when  $r = r^*/1.2$ . Therefore, these stresses were divided by 1.44 to estimate the magnitude of  $\sigma_{11}$  at  $r^*$ . This adjustment is based on the assumption that these stresses vary inversely as the square of the radius. These results are also included in Table I.

The strengths of specimens that were not impacted were measured and averaged 91 MPa. Therefore, the fracture stresses at which the Hertz cracks form are several times the strength of the original material. These higher stresses reflect the fact that the stresses decrease rapidly with depth thus decreasing the stress intensity, the impacts do not usually occur near a severe flaw and there is less sub-critical crack growth under impact conditions.

The flaw sizes can be estimated using the method suggested by Krohn and Hasselman<sup>(13)</sup> who, assuming semi-circular surface flaws, calculated a mirror radius-flaw size ratio of 10. Flaw sizes calculated using this ratio are included in Table I.

### Conclusions

Detailed observations of Hertz cracks formed on surfaces by impacts of glass spheres on glass plates have shown that the shapes of the cracks are very complex and include partial, complete and spiral cracks. Crack branching is common and is clearly revealed by etching of the surfaces with hydrofluoric acid. The fracture stresses at which the Hertz cracks



Table I. Estimated fracture stress and flaw size for fracture origins of Hertz cracks.

Spec. No.	Applied(1) Stress MPa	Impact Velocity $\text{ms}^{-1}$	Contact Radius $r_{\text{max}}$ $\mu\text{m}$	Hertz Crack Radius ( $r^*$ ) $\mu\text{m}$	Crack Length at Branching ( $a_B$ ) $\mu\text{m}$	Est. (2) Fracture Stress MPa	Calc. (3) Fracture Stress MPa	Est. Flaw Size $\mu\text{m}$
3	0	76	530	260	120 <sup>(4)</sup>	228	406	12
6	43.1C	45	320	270	40 <sup>(4)</sup>	395	422	4
11	57.5T	39	340(?)	350	20 <sup>(5)</sup>	559	547	2
35	57.5C	55	420	380	60 <sup>(4)</sup>	323	594	6

Note:

- (1) T indicates tensile, biaxial flexural stress, C indicates compressive stress.
- (2) Crack branching method.
- (3) Ideal static stress assuming  $r = r^*/12$ .
- (4)  $a_B$  measured on impact surface.
- (5)  $a_B$  measured on side of Hertz cone crack.

form were estimated from measurements of the radii at crack branching. To do this it was necessary to assume that the radial tensile stresses controlled the fracture process. The estimated fracture stresses ranged from 228-559 MPa, sometimes less than the calculated radial stresses but substantially greater than the measured strengths of the glass plates. Improvements in the method, especially to take account of the angle at which the crack is inclined to the surface, can be expected to yield improved results. The present results show that fractographic examinations of localized impact damage caused by blunt objects can aid in understanding the mechanisms by which the damage occurs.

#### Acknowledgements

This research was sponsored by the Office of Naval Research.

#### References

1. Lawn, B. and Wilshaw, R., J. Mater. Sci. 10, 1975, 1049.
2. Kirchner, H. P. and Gruver, R. M., Ceramic Finishing Company Tech. Rep. No. 4, Contract N00014-74-C-0241 (1976).
3. Congleton, J. and Petch, N. J., Phil. Mag. 16, 1967, 749.
4. Kirchner, H. P. and Gruver, R. M., Phil. Mag. 27, 1973, 1433.
5. Mecholsky, J. J., Rice, R. W., and Freiman, S. W., J. Amer. Ceram. Soc. 57, 1974, 440.
6. Kirchner, H. P., Gruver, R. M. and Sotter, W. A., J. Amer. Ceram. Soc. 58, 1975, 188.
7. Kirchner, H. P., Gruver, R. M. and Sotter, W. A., Phil. Mag. 33, 1976, 775.

8. Kirchner, H. P., Proceedings of the Second International Conference on Mechanical Properties of Materials, Boston (August, 1976) p. 1317.
9. Evans, A. G., Wilshaw, T. R., Chesnutt, J. C. and Nadler, H., Rockwell International Science Center First Report, Contract N00014-75-C-0669 (1976).
10. Kirchner, H. P. and Sotter, W. A., Ceramic Finishing Company Technical Report No. 1, Contract N00014-74-C-0241 (1974).
11. Lawn, B. R. and Wilshaw, T. R., "Fracture of Brittle Solids," Cambridge University Press, New York, 1975, 20.
12. Evans, A. G., J. Amer. Ceram. Soc. 56, 1973, 405.
13. Krohn, D. A. and Hasselman, D. P. H., J. Amer. Ceram. Soc. 54, 1971, 411.

## BASIC DISTRIBUTION LIST

October 1976

## Technical and Summary Reports

<u>Organization</u>	<u>Number of Copies</u>	<u>Organization</u>	<u>Number of Copies</u>
Defense Documentation Center Cameron Station Alexandria, Virginia 22314	(12)	Naval Construction Battalion Civil Engineering Laboratory Port Hueneme, California 93043 Attention: Materials Division	(1)
Office of Naval Research Department of the Navy Attention: Code 471 Code 102 Code 470	(1) (1) (1)	Naval Electronics Laboratory Center San Diego, California 92152 Attention: Electron Materials Sciences Division	(1)
Commanding Officer Office of Naval Research Branch Office 495 Summer Street Boston, Massachusetts 02210	(1)	Naval Missile Center Materials Consultant Code 3312-1 Point Mugu, California 93041	(1)
Commanding Officer Office of Naval Research Branch Office 536 South Clark Street Chicago, Illinois 60605	(1)	Commanding Officer Naval Surface Weapons Center White Oak Laboratory Silver Spring, Maryland 20910 Attention: Library	(1)
Office of Naval Research San Francisco Area Office 760 Market Street, Room 447 San Francisco, California 94102 Attention: Dr. P. A. Miller	(1)	David W. Taylor Naval Ship R&D Center Materials Department Annapolis, Maryland 21402	(1)
Naval Research Laboratory Washington, D.C. 20390 Attention: Code 6000 Code 6100 Code 6300 Code 6400 Code 2627	(1) (1) (1) (1) (1)	Naval Undersea Center San Diego, California 92132 Attention: Library	(1)
Naval Air Development Center Code 302 Warminster, Pennsylvania 18974 Attention: Mr. F. S. Williams	(1)	Naval Weapons Center China Lake, California 93555 Attention: Library	(1)
Naval Air Propulsion Test Center Trenton, New Jersey 08628 Attention: Library	(1)	Naval Postgraduate School Monterey, California 93940 Attention: Mechanical Engineering Department	(1)
		Naval Air Systems Command Washington, D.C. 20360 Attention: Code 52031 Code 52032 Code 320	(1) (1) (1)



## BASIC DISTRIBUTION LIST (continued)

October 1976

<u>Organization</u>	<u>Number of Copies</u>	<u>Organization</u>	<u>Number of Copies</u>
Naval Sea System Command Washington, D.C. 20362 Attention: Code 035	(1)	NASA Headquarters Washington, D.C. 20546 Attention: Code RRM	(1)
Naval Facilities Engineering Command Alexandria, Virginia 22331 Attention: Code 03	(1)	NASA Lewis Research Center 21000 Brookpark Road Cleveland, Ohio 44135 Attention: Library	(1)
Scientific Advisor Commandant of the Marine Corps Washington, D.C. 20380 Attention: Code AX	(1)	National Bureau of Standards Washington, D.C. 20234 Attention: Metallurgy Division Inorganic Materials Division	(1)
Naval Ship Engineering Center Department of the Navy CTR BG #2 3700 East-West Highway Prince Georges Plaza Hyattsville, Maryland 20782 Attention: Engineering Materials and Services Office Code 6101	(1)	Defense Metals and Ceramics Information Center Battelle Memorial Institute 505 King Avenue Columbus, Ohio 43201	(1)
Army Research Office Box CM, Duke Station Durham, North Carolina 27706 Attention: Metallurgy and Ceramics Division	(1)	Director Ordnance Research Laboratory P.O. Box 30 State College, Pennsylvania 16801	(1)
Army Materials and Mechanics Research Center Watertown, Massachusetts 02172 Attention: Res. Programs Office (AMXMR-P)	(1)	Director Applied Physics Laboratory University of Washington 1013 Northeast Fortieth Street Seattle, Washington 98105	(1)
AirForce Office of Scientific Research Building 410 Bolling Air Force Base Washington, D.C. 20332 Attention: Chemical Science Directorate	(1)	Metals and Ceramics Division Oak Ridge National Laboratory P.O. Box X Oak Ridge, Tennessee 37380	
Electronics and Solid State Sciences Directorate	(1)	Los Alamos Scientific Laboratory P.O. Box 1663 Los Alamos, New Mexico 87544 Attention: Report Librarian	(1)
Air Force Materials Lab (LA) Wright-Patterson AFB Dayton, Ohio 45433		Argonne National Laboratory Metallurgy Division P.O. Box 229 Lemont, Illinois 60439	(1)

## BASIC DISTRIBUTION LIST (Continued)

October 1976

<u>Organization</u>	<u>Number of Copies</u>
Brookhaven National Laboratory Technical Information Division Upton, Long Island New York 11973 Attention: Research Library	(1)
Library Building 50 Room 134 Lawrence Radiation Laboratory Berkeley, California	(1)

SUPPLEMENTARY DISTRIBUTION LIST

ER  
October 1976

Technical and Summary Reports

Dr. W. F. Adler  
Effects Technology, Inc.  
5383 Hollister Avenue  
P.O. Box 30400  
Santa Barbara, CA 92105

Dr. G. Bansal  
Battelle  
505 King Avenue  
Columbus, OH 43201

Dr. S. A. Bortz  
IITRI  
10 West 35th Street  
Chicago, IL 60616

Dr. J. D. Buch  
Prototype Development Assoc., Inc.  
1740 Garry Avenue, Suite 201  
Santa Ana, CA 92705

Dr. B. Budiansky  
Harvard University  
Department of Engineering and Applied Science  
Cambridge, MA 02138

Professor H. Conrad  
University of Kentucky  
Materials Department  
Lexington, KY 40506

Dr. A. Cooper  
Case Western Reserve University  
Materials Department  
Cleveland, OH 44106

Dr. N. Corney  
Ministry of Defence  
The Adelphi  
John Adam Street  
London WC2N 6BB  
UNITED KINGDOM

Dr. A. G. Evans  
Rockwell International  
P.O. Box 1085  
1049 Camino Dos Rios  
Thousand Oaks, CA 91360

Professor John Field  
University of Cambridge  
New Cavendish Laboratory  
Cambridge  
UNITED KINGDOM

Dr. I. Finney  
University of California  
Berkeley, CA 94720

Mr. A. A. Fyall  
Royal Aircraft Establishment  
Farnborough, Hants  
UNITED KINGDOM

Dr. L. M. Gillin  
Aeronautical Research Laboratory  
P.O. Box 4331  
Fishermen's Bend  
Melbourne, VIC 3001  
AUSTRALIA

Dr. M. E. Gulden  
International Harvester Company  
Solar Division  
2200 Pacific Highway  
San Diego, CA 92138

Professor A. H. Heuer  
Case Western Reserve University  
University Circle  
Cleveland, OH 44106

Dr. R. Hoagland  
Battelle  
505 King Avenue  
Columbus, OH 43201

## SUPPLEMENTARY DISTRIBUTION LIST (continued)

ER  
October 1976

Dr. R. Jaffee  
Electric Power Research Institute  
Palo Alto, CA

Dr. R. N. Katz  
Army Materials and Mechanics  
Research Center  
Watertown, MA 02171

Dr. H. Kirchner  
Ceramic Finishing Company  
P.O. Box 498  
State College, PA 16801

Dr. B. Koepke  
Honeywell, Inc.  
Corporate Research Center  
500 Washington Avenue, South  
Hopkins, MN 55343

Mr. Frank Koubek  
Naval Surface Weapons Center  
White Oak Laboratory  
Silver Spring, MD 20910

Dr. F. F. Lange  
Westinghouse Electric Corporation  
Research Laboratories  
Pittsburgh, PA 15235

Dr. J. Lankford  
Southwest Research Institute  
8500 Culebra Road  
San Antonio, TX 78284

Dr. B. R. Lawn  
Physics Department  
University New South Wales  
Kingston, New South Wales  
AUSTRALIA

State University of New York  
College of Ceramics at Alfred University  
Attention: Library  
Alfred, NY 14802

Dr. R. E. Loehman  
University of Florida  
Ceramics Division  
Gainesville, FL 32601

Dr. N. MacMillan  
Materials Research Laboratory  
Pennsylvania State University  
College Park, PA 16802

Mr. F. Markarian  
Naval Weapons Center  
China Lake, CA 93555

Dr. F. A. McClintock  
Massachusetts Institute of Technology  
Department of Mechanical Engineering  
Cambridge, MA 02139

Dr. Perry A. Miles  
Raytheon Company  
Research Division  
28 Seyon Street  
Waltham, MA 02154

Dr. D. Mulville  
Office of Naval Research  
Code 474  
800 North Quincy Street  
Arlington, VA 22217

Dr. N. Perrone  
Office of Naval Research  
Code 474  
800 North Quincy Street  
Arlington, VA 22217

Dr. J. R. Rice  
Brown University  
Division of Engineering  
Providence, RI 02912

Dr. R. Rice  
Naval Research Laboratory  
Code 6360  
Washington, DC 20375



## SUPPLEMENTARY DISTRIBUTION LIST (continued)

ER  
October 1976

Professor R. Roy  
Pennsylvania State University  
Materials Research Laboratory  
University Park, PA 16802

Dr. L. Rubin  
Aerospace Corporation  
P.O. Box 92957  
Los Angeles, CA 90009

Dr. G. Schmidt  
Air Force Materials Laboratory  
Wright-Patterson AFB  
Dayton, OH 54533

Dr. D. A. Shockey  
Stanford Research Institute  
Poulter Laboratory  
Menlo Park, CA 94025

Dr. R. A. Tanzilli  
General Electric Company  
Reentry and Environmental Systems Division  
3198 Chestnut Street  
Philadelphia, PA 19101

Dr. T. Vasilos  
AVCO Corporation  
Research and Advanced Development Division  
201 Lowell Street  
Wilmington, MA 01887

Dr. S. M. Wiederhorn  
Inorganic Materials Division  
National Bureau of Standards  
Washington, DC 20234